Computational Identification of Ternary Wide-Band-Gap Oxides for High-Power Electronics

Emily M. Garrity,[1,2] Cheng-Wei Lee,[1,2] Prashun Gorai,[1,2] M. Brooks Tellekamp,[2] Andriy Zakutayev,[2] and Vladan Stevanović[1,2,*]

[1] *Colorado School of Mines, Golden, Colorado 80401, USA*

[2] *National Renewable Energy Laboratory (NREL), Golden, Colorado 80401, USA*

(Received 8 March 2022; revised 31 October 2022; accepted 15 November 2022; published 20 December 2022)

As electricity grids become more renewable energy compliant, there will be a need for novel semiconductors that can withstand high power, high voltage, and high temperatures. Currently used or explored wide-band-gap materials for power electronics are costly (GaN), difficult to synthesize as high-quality single crystals (SiC) and at scale (diamond, BN), have low thermal conductivity (β-Ga_2O_3), or cannot be suitably doped (AlN). We conduct a computational search for novel semiconductors across 1340 known metal oxides using first-principles calculations and existing and improved transport models. We calculate the Baliga figure of merit (BFOM) and lattice thermal conductivity (κ_L) to identify top candidates for *n*-type power electronics. We find 47 mostly ternary oxides that have higher κ_L than β-Ga_2O_3 and higher *n*-type BFOM than SiC and GaN. We use the branch point energy to rank the likelihood of *n*-type extrinsic doping, further reducing our top candidates to 14 previously unexplored compounds. Among these, several material classes emerge, including 2-2-7 stoichiometry thortveitites and pyrochlores, II-IV spinels, and calcite-type borates. Within these classes, we propose $In_2Ge_2O_7$, Mg_2GeO_4, and $InBO_3$ for power electronics as they are the most favorable for *n*-type doping based on our preliminary evaluation and could be grown as single crystals or thin-film heterostructures.

DOI: 10.1103/PRXEnergy.1.033006

I. INTRODUCTION

Increased electrification, smart grid technology, and renewable power generation has brought to light the need for improved power electronics. These are required for an electrical grid that is more sustainable, flexible, reliable, and distributed [1,2]. As technologies like photovoltaics and electric vehicles become more common at the utility scale, the electronics for power conversion (dc to ac, ac to dc) must be able to handle larger power [3]. In addition, traditionally analog technologies like transformers used in power transmission can be replaced by solid-state inverters that allow the quick transfer of distributed, renewable energy across long geographical distances [3]. These applications require power electronics that can handle high voltages with great efficiency while keeping device size relatively small [4].

As a consequence of high-power (kilowatts to gigawatts and more) and high-voltage (> 1200 V per component) requirements, any new power electronic device must also withstand elevated temperatures [3,5]. One can address this need for better devices by either engineering new architectures around existing semiconductors or replacing the semiconductor with an inherently higher-performing material. In this paper we focus on the latter: the identification of previously unexplored semiconductors for future power electronics.

The semiconductors currently used for power applications sample a small portion of the materials that exist today. Their measured performance in low-frequency vertical devices as characterized by the well-known Baliga figure of merit [8] is shown in Fig. 1 along with other indicators of performance and commercialization like the maximum realized carrier concentration at room temperature, thermal conductivity, and achievable wafer size. Silicon remains dominant in commercial power devices as a consequence of decades of research into economical and large-scale manufacturing processes. However, with a small critical electric field at breakdown [1], silicon is

*vstevano@mines.edu

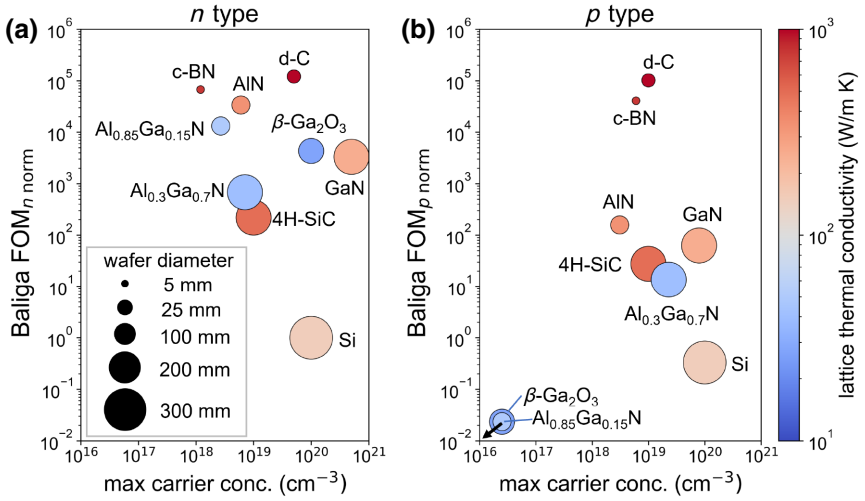

FIG. 1. The *n*-type (a) and *p*-type (b) performance of commercialized and exploratory power electronic semiconductors in terms of the Baliga figure of merit (relative to *n*-type Si), thermal conductivity, and maximum reported carrier concentration at room temperature. The size of the circle indicates maximum achieved single-crystal wafer size. Normalized Baliga figure of merit calculated using measured quantities in state-of-art devices. Arrow near Ga_2O_3 and $Al_{0.85}Ga_{0.15}N$ indicates that there are no known reports of room-temperature *p*-type doping concentrations or measured hole mobility (and therefore *p*-type BFOM) for these materials. Most data are obtained from Refs. [1,6] and supplemented by material-specific data as listed in Table S-I within the Supplemental Material [7].

hitting its theoretical performance limit within reasonable device size and power losses.

Currently used alternatives to silicon include wide-band-gap ($1.5 < E_g < 3.4$ eV) semiconductors such as GaN and SiC that offer significantly improved performance and smaller device size. The move toward wider-band-gap materials signifies a marked improvement in energy savings. For example, wide-band-gap metal-oxide-semiconductor field-effect transistors cut heat losses by half as they increase efficiency from 96% to 98% compared to Si-based devices [6]. As shown in Fig. 1, the wide- and ultra-wide-band-gap ($E_g > 3.4$ eV) alternatives have Baliga figures of merit capable of addressing the demands of the future energy grid, especially *n*-type devices. Unfortunately, considering only the semiconductor performance is not sufficient in determining commercial success. One must also consider other relevant factors like the ability to be doped (preferably both *n* and *p* types), the ability to make high-quality crystals with large wafer size, and the ability to dissipate heat when operating at high power. For many of these materials, addressing these deficiencies is still a work in progress.

The handful of promising wide-band-gap (WBG) and ultra-wide-band-gap (UWBG) power electronics in Fig. 1 have resulted from decades of research into semiconductors. With the exception of (Al,Ga)N alloys, all are binary compounds. Considering the many other binary as well as ternary and quaternary compounds that exist, one wonders whether there are other better-performing semiconductors that have yet to be investigated.

Previous works that have proposed new WBG and UWBG semiconductors beyond those in Fig. 1 often focus on one or two promising materials. Rutile GeO_2 was recently predicted to be an UWBG semiconductor with high electron mobility, ambipolar doping, and a Baliga figure of merit that surpasses current technologies [9,10]. However, this performance has yet to be realized in real devices due to difficulty in thin-film synthesis [11,12]. Calculations have shown that metastable rocksalt ZnO is ambipolarly dopable unlike its ground-state wurtzite version [13], but experiments have yet to realize it. For these exploratory materials, single-crystal growth, extrinsic doping, and device integration remain to be investigated.

Researchers have also begun to explore beyond traditional binary semiconductors, expanding to ternary UWBG compounds. Spinel Ga_2ZnO_4 [14] and inverse spinel Ga_2MgO_4 [15] can be melt processed in bulk and doped *n* type, but their lattice thermal conductivities are lower than that of β-Ga_2O_3. $LiGaO_2$ is another UWBG material that is predicted to be *n*-type dopable with Si or Ge, but experimental investigation of achievable carrier concentration is needed to prove its potential [16,17].

A more comprehensive computational search for novel power semiconductors was recently performed by Gorai *et al.* [18]. They considered a select list of 863 sulfides, nitrides, carbides, silicides, borides, and oxides and evaluated the Baliga figure of merit and thermal conductivity using high-throughput first-principles calculations. This screening identified a number of theoretically high-performing candidates, but did not systematically address

whether these materials can be extrinsically doped to desired concentrations. The *n*-type dopability, as determined by formation energy calculations of compensating native defects, was assessed for only a few select materials. But to fully understand which materials of the many candidates should be prioritized in experiments, one needs additional screening criteria.

In this work we cast a wide net in the search for new *n*-type power electronics among binary, ternary, and quaternary compounds. We use a combination of high-throughput screening using density functional theory (DFT) calculations and a more thorough analysis of top compounds to find new power electronic candidates from the Inorganic Crystal Structures Database (ICSD) [19]. This study is focused on oxides because they have the advantage of not oxidizing at high temperatures. Single crystals of oxides could also be easier to grow, as evidenced by β-Ga_2O_3 [20]. In addition, we focus on searching for *n*-type candidates given most known metal-oxide semiconductors show electron conduction [21,22] and commercial power devices utilize *n*-type Si, SiC, and GaN over *p* type. We evaluate the performance of an extended list of oxides via the Baliga figure of merit (BFOM) and lattice thermal conductivity calculated using DFT and updated semiempirical transport models. We confirm the DFT results with a more accurate hybrid exchange-correlation functional (HSE06) on the select set of top DFT candidate materials. We also assess their *n*-type dopability using a qualitative ranking based upon the branch point energy [23,24]. The dopability ranking is validated using modern defect theory and defect formation energy calculations. Lastly, we rely on literature to determine the synthesis history and potential for single-crystal or thin-film growth of these top candidates.

From this study, we have identified three novel families of ternary oxides, which have high theoretical performance based on the combination of their calculated Baliga FOM and thermal conductivity: $(III)_2(IV)_2O_7$ oxides with thortveitite and pyrochlore polymorphs; $(III)_2(II)O_4$ and $(II)_2(IV)O_4$ oxides, most of them adopting the spinel crystal structure; and $(III)BO_3$ borates with the calcite structure. Many of the oxides from these families are also likely *n*-type dopable according to our qualitative ranking. Through investigation of compositional stability and literature on experimental synthesis, we identify the most promising candidates within these families, many of which were previously grown as single crystals or are lattice matched to the common substrates for thin-film growth. Taking into consideration the theoretical performance and potential for growth, we propose a select subset of these oxides, in particular $In_2Ge_2O_7$, Mg_2GeO_4, and $InBO_3$, for further computational and experimental investigation for high-power electronics.

II. COMPUTATIONAL METHODOLOGY

A. Materials screening

The computational workflow used to determine the top performing oxides is shown in Fig. 2. It is divided into two subsections: high-throughput materials screening, and higher-accuracy top candidate evaluation.

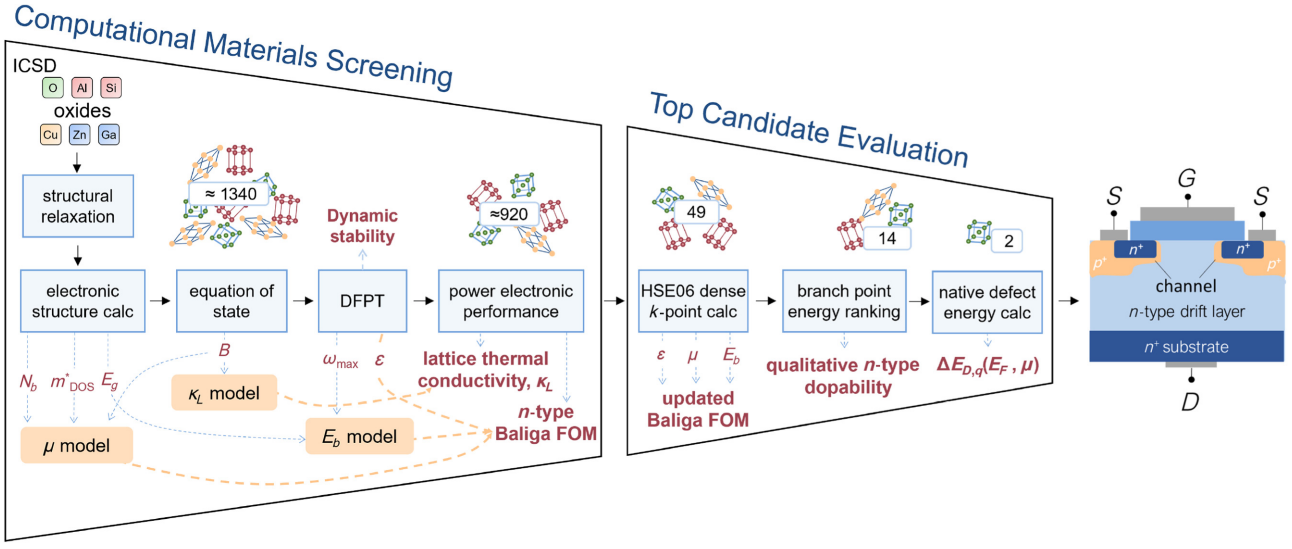

FIG. 2. Computational workflow to identify *n*-type semiconductor oxides for power electronics. The first phase contains high-throughput GGA+U calculations to determine the Baliga FOM and lattice thermal conductivity (κ_L) and to screen the materials. The second phase includes a more accurate calculation of the band structure using the HSE06 hybrid functional for top candidates, a qualitative ranking of *n*-type dopability, and detailed native defect formation energy calculations for two high- and low-ranked candidates.

1. Performance metrics

The materials screening section follows the methods outlined in Gorai *et al.* [18]. We use the well-known Baliga FOM for high-power, high-voltage field-effect transistors as the metric of performance [8]. The Baliga FOM takes into account the carrier mobility (μ), dielectric constant (ε), and critical electric field at breakdown (E_b):

$$\mathrm{BFOM} = \varepsilon \mu E_b^3. \tag{1}$$

The carrier mobility is important for conduction as it is a measure of how easily electrons or holes transport through a material. The dielectric constant and breakdown field set the maximum allowable applied voltage for a device with a given carrier concentration. Maximization of the Baliga FOM is equivalent to minimizing the on-state resistance of a conducting transistor in forward bias and thus indicates the maximum achievable efficiency for low-frequency devices. The BFOM does not, however, take into account the important role of thermal management in high-power devices. The material must be able to quickly dissipate heat generated through power losses. Thus, we use the lattice thermal conductivity (κ_L) as an additional metric to score the performance of our materials.

2. Search space

Binary, ternary, and quaternary crystals containing oxygen as the sole anion are selected from the ICSD as the starting crystal structures [19]. Cations consist of metals and metalloids including likely nonmagnetic transition-metal elements (Sc, Y, La, Cu, Ti, Zr, Hf, Ta, W, Ag, Au, Zn, Cd, Hg) as an extension of the oxide data set generated by Gorai *et al.* [18]. Rare-earth elements and nonmetals other than oxygen are excluded. Only stoichiometric compounds are considered. The search is also limited to compounds with unit cells of 50 atoms or fewer to make the task computationally tractable. There are 378 oxides repeated from Gorai *et al.* and approximately 959 additional transitional metal oxides for a total of about 1340 oxides.

3. Semiempirical models

Direct calculations of the intrinsic mobility, breakdown field, and lattice thermal conductivity are presently possible using first-principles methods. However, computing the electron-phonon and phonon-phonon coupling constants and the resulting scattering rates is intractable for a high-throughput evaluation. Therefore, we determine these quantities through previously validated, semiempirical models that depend on more easily calculated properties.

The semiempirical carrier mobility model was developed in Yan *et al*. [25] and improved in this work. The functional form of the model assesses the intrinsic mobility limits of a material and is motivated by classic electron-phonon scattering mechanisms [26,27] including deformation potential, polar optical phonon, and piezoelectric scattering. Each of these mechanisms depends implicitly on the elastic properties of the material through the displacement of atoms due to phonon-induced deformation, be it the change in electronic eigenvalue or electric field due to polarization. To account for this, we hypothesize a dependence on the bulk modulus in our mobility model. Furthermore, all electron-phonon scattering rates also depend on the electron density of states (DOS), which reflects the number of states available to scatter into. Since, in the parabolic band approximation, the DOS depends on the effective mass as $(m^*)^{3/2}$, and the mobility is inversely proportional to the product of effective mass (m^*) and the scattering rate (inverse relaxation time), the approximate dependence of the mobility on the effective mass is $(m^*)^{-5/2}$. The mobility model is thus

$$\mu = A_0 B (m_b^*)^{-5/2}, \tag{2}$$

where B is the bulk modulus, m_b^* is the band effective mass, and A_0 is a fitted parameter.

To assess the validity of this simple model, we use well-characterized room-temperature electron mobilities across 20 different semiconductors for the lowest doping levels reported in the literature. As seen in Fig. 3, our model (red data) is shown to reproduce intrinsic electron mobility values within typical experimental uncertainties covering narrow-gap systems such as PbTe, medium-gap materials like Si or GaAs, and wide-gap semiconductors like ZnO and GaN. The mobility model, in combination with that describing lattice thermal conductivity, has been successfully used to identify promising thermoelectric materials [28,29] and has led to discoveries of Mg_3Sb_2 [30], $KAlSb_4$, $KGaSb_4$ [31], and various *n*-type Zintl compounds [32].

The intrinsic critical breakdown fields are calculated using a machine-learning model developed by Kim *et al.* [33]. The model is fit using experimental band gaps and *ab initio* calculations of the breakdown field using electron-phonon coupling for 82 dielectric materials [33,34]. The critical breakdown field is calculated as

$$E_b = 24.442\, e^{0.315\sqrt{E_g\,\omega_{\max}}}, \tag{3}$$

where E_g is the band gap in electronvolts and $\omega_{\max}$ is the maximum phonon frequency at the Γ point in terahertz.

Finally, the lattice thermal conductivity is evaluated using a simplified Debye-Callaway model previously validated in Ref. [35]. This model is the sum of both the acoustic and optical phonon contributions, assuming that Umklapp scattering is the dominant mechanism. The model is fit to experimental room-temperature thermal conductivity

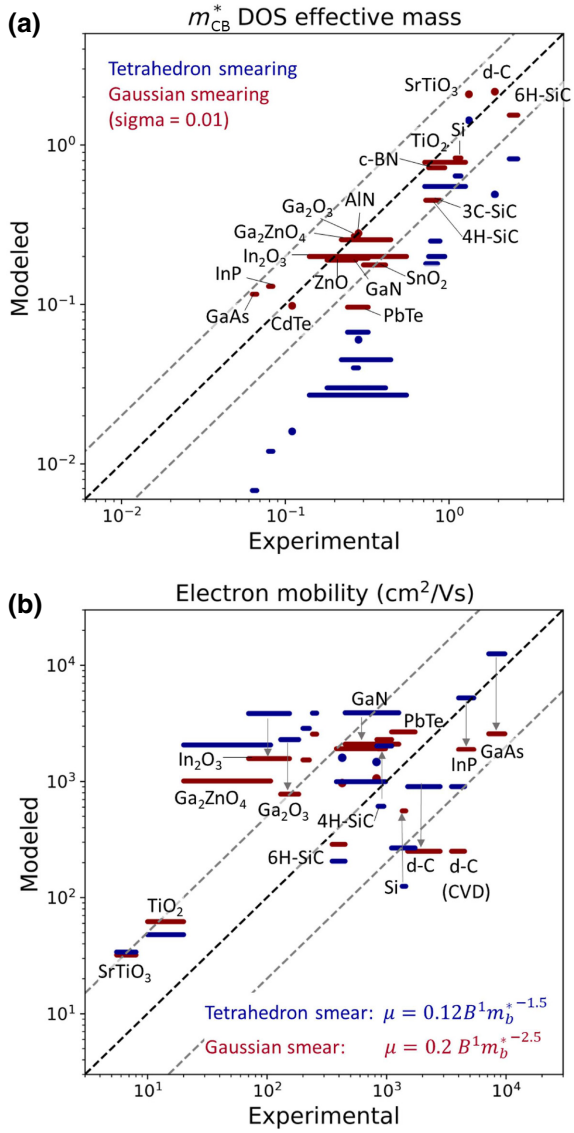

FIG. 3. Prediction accuracy of old and new calculations. (a) Comparison of experimentally measured density of states (DOS) effective mass at the conduction-band edge with two DOS calculation methods. Gaussian smearing is more accurate than tetrahedron smearing. (b) Two fit models for electron mobility: the Yan *et al.* [25] model with $m^*_{\mathrm{DOS,CB}}$ calculated via tetrahedron smearing and our updated model that uses Gaussian smearing. Both models perform equally well at predicting measured room-temperature electron mobility. Dashed lines represent half an order-of-magnitude deviation from average experimental values.

data from 55 compounds that span four orders of magnitude. The lattice thermal conductivity is calculated as

$$\kappa_L = A_1 \frac{M v_s^y}{T\gamma^2 V^z n^x} + A_2 \frac{v_s}{V^z}\left(1 - \frac{1}{n^{2/3}}\right), \tag{4}$$

where M is the average atomic mass, v_s is the speed of sound in m/s, V is the volume per atom, n is the number of atoms in the primitive cell, γ is the Gruneisen parameter, T is the temperature, and A_1, A_2, x, y, z are fitted parameters. The speed of sound is calculated using $v_s \approx \sqrt{B/d}$, where B is the bulk modulus and d is the density of the compound.

4. Calculation methods

Starting structures are relaxed using the Perdew-Burke-Ernzerhof generalized gradient approximation (GGA) [36] in the projector-augmented-wave formalism [37] as implemented in the Vienna *Ab-initio* Simulation Package [38]. A plane-wave cutoff of 340 eV is used and an on-site Hubbard-U correction (GGA+U) is applied, following the methodology outlined in Refs. [39,40]. A uniform parameter of $U = 3$ eV is used for d states of all transition metals except for Ag and Cu for which $U = 5$ eV is used. These values have been previously determined by Stevanovic *et al.* [41] for the purpose of computing accurate enthalpies of formation.

Once relaxed, the electronic structure is calculated using a k-point grid density of $N \times n_{\mathrm{kpts}} = 8000$, where N is the number of atoms in the primitive cell and n_{kpts} is the number of k points. The band gap is obtained from the dense k-point electronic structure. At this point in the workflow, 272 compounds with $E_g = 0$ are removed from subsequent calculations since high-performing materials will need to have large band gaps.

The density of states effective mass for electrons ($m^*_{\mathrm{DOS,CB}}$) is calculated from the DOS of the dense k-point calculation within a 100-meV window from the conduction-band edge using a parabolic band approximation. The conduction-band effective mass ($m^*_{b,\mathrm{CB}}$) is then calculated as $m^*_{\mathrm{DOS,CB}} = N_b^{2/3} m^*_{b,\mathrm{CB}}$, where N_b is the band degeneracy, or number of charge carrier pockets, within the energy window. Our expression for m^*_b is, strictly speaking, valid for symmetry-equivalent and isotropic (spherical) charge carrier pockets. However, these assumptions facilitate robust high-throughput calculations as they eliminate the need for fitting the curvature of individual bands, a process that can be numerically challenging given that it requires identifying extremal points and generating sufficiently dense k-point grids around those points.

This same m^*_b calculation method was used in Yan *et al.* [25] and Gorai *et al.* [18] as inputs to the mobility model [Eq. (2)]. However, upon deeper inspection, the conduction-band effective masses used in these works are severely underestimated compared to experiments, and thus the exponents in the mobility model needed to be adjusted to account for this underestimation. To predict the effective masses more accurately, we use Gaussian smearing (sigma = 0.01) rather than the previous tetrahedron smearing of Yan *et al.* [25] to obtain the density of states near the band edges. The comparison of each smearing method to experimentally derived or carefully calculated $m^*_{\mathrm{DOS,CB}}$ for 20 common semiconductors and oxides is shown in Fig. 3(a) (see also Table S-II within

the Supplemental Material [7]). Gaussian smearing more accurately captures the appearance of distinct states close to the band edge and is thus, according to our calculations, more suitable for calculating $m^*_{\mathrm{DOS,CB}}$ within the accuracy of experiments. The resulting $m^*_{b,\mathrm{CB}}$ also aligns well with experiments. For example, the predicted averages $m^*_{b,\mathrm{CB}}$ for GaN and 4H-SiC are 0.19 and 0.22, respectively, consistent with experimental values [42–47].

In addition, the more accurate band effective masses allow us to use the physically derived exponents in the mobility model. As shown in Fig. 3(b), this model performs as well as the previous mobility model in Yan *et al.* [25], predicting room-temperature electron mobilities within about half an order of magnitude of experiments (see Table S-II within the Supplemental Material [7]) for most of the materials considered. When considering a large dataset with predicted mobilities spanning many orders of magnitude, the model is useful in extracting trends between different material systems. Thus, we use Gaussian smearing and the updated mobility model parameters for the electronic structure calculations in this work.

Next, we perform total energy versus volume calculations and fit the Birch-Murnaghan [48,49] equation of state to evaluate the bulk modulus. About 30 materials do not obey the Birch-Murnaghan equation of state, indicating a very shallow or even nonexistent local minimum. These entries are removed from the dataset as they are likely unstable compounds.

Next, a density functional perturbation theory (DFPT) calculation [50,51] is performed at the Γ point only to evaluate the dielectric constant and phonon frequencies. The converged results are obtained using a stricter energy cutoff of 520 eV and k-point grid density of $N \times n_{\mathrm{kpts}} = 1000$. The $\omega_{\max}$ and the directional average of the electronic + ionic contributions to the dielectric tensor (ε) are extracted from the results. A total of 106 compounds have imaginary optical phonon modes, indicating that they are dynamically unstable. These are also removed from the dataset. The starting 1340 structures are reduced to about 920 at the end of the materials screening.

B. Top candidate evaluation

1. Hybrid functional calculations

Compounds with n-type Baliga FOM and κ_L above chosen cutoffs are downselected as top candidates and subjected to more in-depth evaluation. First, a more accurate hybrid functional, HSE06 [52,53], is used to rerelax and calculate the electronic structures. We use a standard mixing parameter of 0.25 and a screening parameter of 0.2 $\mathrm{Å}^{-1}$. While GGA+U is appropriate for high-throughput calculations, it is known to underestimate the band gaps [54]. We choose to invest in higher-accuracy hybrid calculations as additional verification of the BFOM ranking results. The calculation of electronic structure with HSE06 is an average of 1000 times more expensive than GGA+U. Therefore, we save these calculations for only the top candidates after screening with less computationally expensive methods. The equation of state calculations are not rerun with HSE06 since preliminary tests showed that bulk modulus calculated with the higher-accuracy method did not significantly impact Baliga figures of merit (see Table S-V within the Supplemental Material [7]).

2. n-type dopability ranking

Next, the top candidates are ranked according to a first-order approximation of their ability to be doped n type. Typically, n-type dopability is assessed by calculating the formation energies of native compensating acceptor defects relative to the Fermi energy of the electron-doped material [55]. Because calculations of defect formation energies are computationally expensive, this approach is not tractable for close to 50 materials. Instead, we use the branch point energy based on the HSE06 band structure as a proxy for n-type dopability.

The branch point energy (E_{BP}), also known as the charge neutrality level, provides an estimate of the intrinsic Fermi level based upon averaging of the conduction- and valence-band dispersions. The work of Woods-Robinson *et al.* [56] showed that a branch point energy inside or close to the conduction band is correlated with n-type dopability for many ionic oxide compounds, including ternaries. This qualitative descriptor works particularly well for determining materials that are only n-type dopable (not p-type dopable). For branch point energies near the midgap or valence-band edge, the relationship to dopability is inconclusive. Without more information, it is not possible to determine whether a material is ambipolar dopable, p-type dopable, or an insulator. Therefore, this descriptor can be used to screen for materials that are most likely to favor n-type doping although it may miss a few ambipolar dopable candidates.

We compute E_{BP} from the HSE06 full band structure as

$$E_{\mathrm{BP}} = \frac{1}{2N_k}\sum_k \left(\frac{1}{N_{\mathrm{CB}}}\sum_i^{N_{\mathrm{CB}}} \varepsilon_i(k) + \frac{1}{N_{\mathrm{VB}}}\sum_j^{N_{\mathrm{VB}}} \varepsilon_j(k)\right), \quad (5)$$

where N_k is the number of k points, the ε_i are the eigenvalues at each k point, and N_{CB} and N_{VB} are the chosen numbers of conduction and valence bands included in the averaging.

Shapera and Schleife [57] found that using N_{VB}=$N_e/4$ and N_{CB}=$N_e/8$ produced the lowest mean absolute error between computed and experimental E_{BP}. Here N_e is the total number of valence electrons from the s and p orbitals per formula unit. Their comparison was conducted on mostly binary compounds with one cation, where a simple picture of contributing orbitals will follow a ratio of $N_{\mathrm{VB}} : N_{\mathrm{CB}} = 2 : 1$. Given the appearance of many ternary

and quaternary compounds in our dataset, we also consider other ratios in order to quantify the inherent error in the choice of the number of bands. The $N_{VB} : N_{CB}$ ratios included here are $N_e/8 : N_e/8$, $N_e/2.66 : N_e/8$, $N_e/2.66 : N_e/4$, and $N_e/3 : N_e/6$. In the case of fractional bands, the number of included bands is rounded up to the nearest integers that maintained the desired $N_{VB} : N_{CB}$ ratio.

3. Native defect calculations

Once ranked, the *n*-type dopability of one top and one bottom candidate from the qualitative assessment is evaluated using detailed defect formation energy calculations of all relevant native point defects (vacancies, interstitials, antisites). We follow the standard supercell approach to calculate the formation energy ($E_{D,q}$) of the defect D in the charge state q as a function of Fermi energy (E_F) and at various chemical potentials (μ) [55,58]. We use an 88-atom supercell with a $2 \times 2 \times 2$ k-point mesh for pyrochlore $In_2Ge_2O_7$ and a 297-atom supercell with gamma only mesh for $CaZrSi_2O_7$. The defect supercells are relaxed with DFT GGA (+U, $U = 3.0$ for Zr) using a plane-wave cutoff energy of 340 eV and a force convergence criterion of 5 meV/Å. Furthermore, self-consistent *GW* calculations with fixed wave functions [59] are performed to correct the band-gap error of GGA+U. The chemical potentials are calculated using the fitted elemental-phase reference energy approach [41]. Static dielectric constants of 21.85 and 10.68 are calculated using GGA+U and are used for the image-charge correction [55] for $In_2Ge_2O_7$ and $CaZrSi_2O_7$, respectively.

4. Synthesis evaluation

Lastly, we study the literature for indication of previous synthesis of these materials. This is especially important for those compounds that are not ground-state materials as they may decompose to competing phases. In these cases we look for evidence of synthesis and ambient condition stability through high-pressure and quenching techniques. In addition, we note any published demonstration of single-crystal growth as this could allow bulk growth of native substrates. For select top candidates, we also gauge the possibility of epitaxial growth of thin-film heterostructures by comparing the lattice constants of the candidate compound and well-known substrates. Understanding material stability and synthesis is key in prioritizing which materials to investigate further with experimental efforts.

III. PERFORMANCE METRIC RESULTS

A. Materials screening: DFT-GGA calculations

Using the structure selection criteria, we start with a total of around 1340 oxide crystals from the ICSD. After completing the high-throughput DFT workflow, there are about 920 remaining structures that are dynamically stable and have finite band gaps. The thermal conductivity versus Baliga FOM for all calculated structures is plotted in Fig. 4. The axes limits have been chosen to magnify the results of the best performers. Baliga figure of merit values have been normalized to *n*-type Si calculated with GGA+U (Si $BFOM_{n-norm} = 1$). Commercially used (GaN, SiC, Si) and previously proposed (β-Ga_2O_3, BN, AlN, diamond) power electronic (PE) semiconductors are indicated with the squares as a reference. The reference materials follow the expected trends. Si has the lowest BFOM, β-Ga_2O_3 has the lowest κ_L, and diamond and cubic BN perform an order of magnitude above the rest of the reference materials in both measures.

When one considers the important commercialization factors beyond the figure of merit, it becomes clearer that new alternatives to common power electronic materials would be helpful. Despite the theoretical potential for high performance, diamond's application in power electronics is limited by its small wafer size, extreme fabrication costs, high dislocation densities, and lack of high-quality substrates for epitaxial growth [6]. Historically, AlN has been limited by difficulties with doping [6,60]. Both *n*-type doping with Si and *p*-type doping with Be to 10^{18} cm^{-3} are recent achievements that have been used to demonstrate a *p*-*n* homojunction diode with nearly ideal turn-on voltage [61,62]. Despite this achievement, commercialization of AlN devices is still limited by the lack of large, doped bulk substrates [6,60]. Cubic BN suffers from similar substrate challenges [6]. Low Al content (Al,Ga)N has the potential for growth on GaN substrates, albeit with some concern for interface strain, but does not provide significant performance advantages over other WBG materials [6,63]. High Al content $Al_{0.85}Ga_{0.15}N$ is more appropriate for high-power vertical devices, but has limited wafer size and has not yet been proven *p*-type conductive due to the high activation energy of Mg dopants [6,64,65]. Even GaN and 4H-SiC, which are the state-of-the-art choices for high-frequency and high-power electronics, respectively, have their challenges. SiC is still relatively costly to produce with low defect densities [3,5]. GaN can be grown on 200-mm Si substrates but lacks decent-sized vertical devices grown on native substrates that are critical for high-power applications [5].

Our search results identify plenty of potential materials that could complement and compete with current power electronic semiconductors. To downselect, we set the top candidate cutoff values at GaN for $BFOM_{n-norm}$ and β-Ga_2O_3 for κ_L plus a margin. Using this criteria, we identify 49 oxides with $BFOM_{n-norm} > 10$ and $\kappa_L > 16$ W/mK, which are plotted in the top right region of Fig. 4. A few interesting families of materials, which are discussed in detail later, are labeled as well. Of these top candidates, 80% are ternaries, despite them making up 55% of the dataset. Given that most incumbent materials are

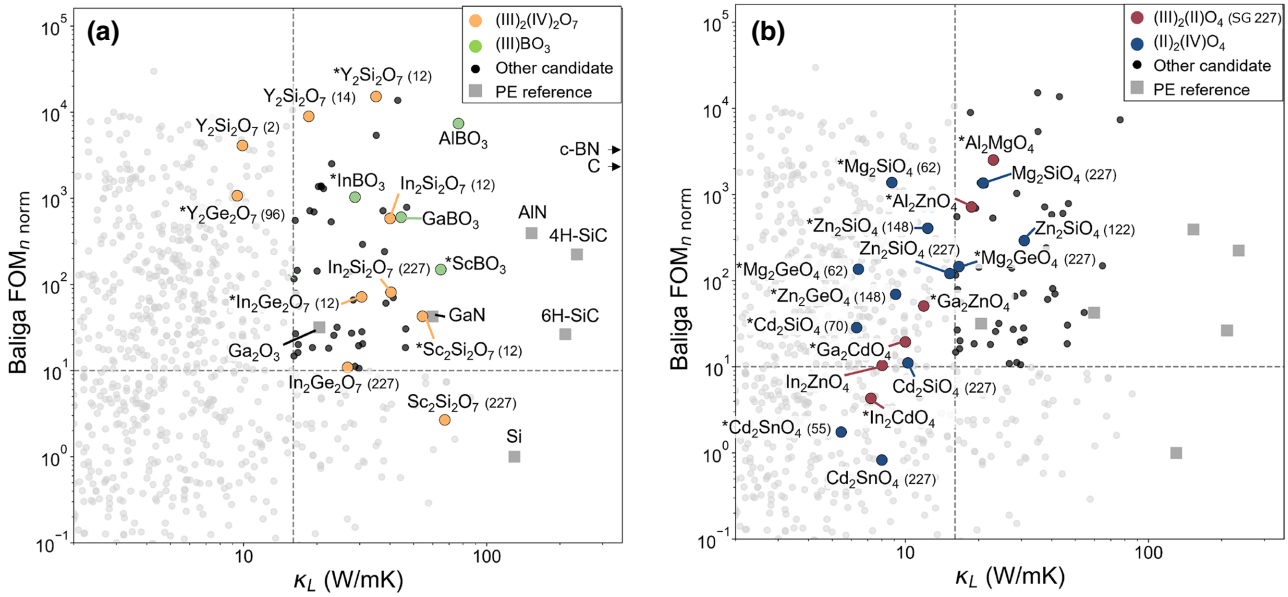

FIG. 4. Baliga figure of merit for *n*-type power electronic performance (normalized to *n*-type Si) and lattice thermal conductivity of oxides calculated with the GGA+U method. Highlighted top candidates (upper right quadrant) include members of one known, $(III)_2(II)O_4$ spinel (right), and three newly identified families of materials, $(III)BO_3$ calcite (left), $(III)_2(IV)_2O_7$ (left), and $(II)_2(IV)O_4$ (right) for power electronics. Numbers [e.g., (227)] represent the international space group (SG) number of the structure. Asterisks denote ground-state materials that lie on the convex hull.

binary compounds, the discovery of so many promising ternary compounds points to the impact that a broader computational search can have on next-generation power electronics.

B. Top candidate evaluation: HSE06 calculations

To confirm the best candidates, the band structure properties of the top 49 candidates and reference materials are recalculated using the HSE06 hybrid functional. This is especially relevant given the known underestimation of GGA+U band gaps and the importance of the band gap in the calculation of the Baliga FOM. Hybrid functionals also produce more accurate electronic density of states, especially for compounds with transition-metal *d*- and *f*-orbital states at the conduction-band edge that tend to be made overly dispersive by GGA+U. Figure 5 shows the parallel coordinate plot of the HSE06-calculated values (E_g, $m^*_{b,\mathrm{CB}}$, E_b, μ_n, $\mathrm{BFOM}_{n-\mathrm{norm}}$) for the governing material properties that make up the *n*-type Baliga FOM. The top 49 candidates are plotted in a gradient blue according to $\mathrm{BFOM}_{n-\mathrm{norm}}$ that have been normalized to the HSE06-calculated Si value and reference materials are presented in magenta (see also Tables S-III and S-IV within the Supplemental Material [7]).

Let us first consider how the predictions have changed with the use of HSE06 instead of GGA+U methods. By using the higher-accuracy functional, band gaps increased by up to 2.6 eV in all of the materials. In addition, many materials containing transition-metal elements had lower mobility with the HSE06 method. However, given the heavy influence of the band gap on the BFOM, all but four materials showed a higher normalized Baliga FOM with HSE06 compared to the GGA+U values. $GeHfO_4$ had an order-of-magnitude increase in $m^*_{b,\mathrm{CB}}$, yet remained a top candidate despite a smaller HSE06 $\mathrm{BFOM}_{n-\mathrm{norm}}$ of 92. $TiAl_2O_5$ and $TiGa_4O_8$ also saw a significant decrease in predicted mobility, likely due to the correction of GGA+U exaggerated dispersions of Ti *d*-states at the conduction-band edge. Given their low HSE06 $\mathrm{BFOM}_{n-\mathrm{norm}}$ values, we eliminate these two materials from the top candidate list and move forward with the remaining 47 compounds.

Diving deeper into the results, let us inspect the relative influence of each material property on the top candidates. The normalized *n*-type BFOM of the top candidates spans 4 orders of magnitude. Despite the Baliga FOM's heavy dependence on the band gap, the top candidates span a wide range of E_g from a moderate 2 eV to very ultrawide 8.2 eV. The materials with band gaps smaller than GaN (calculated as 3.3 eV) like $CuTaO_3$ and $TiHgO_3$ make up for this with high dielectric constants that contribute to Baliga figures of merit above 100. This suggests that it may be necessary to rethink the recent strong emphasis on ultrawide band gaps as the sole criteria for new candidates, as these compounds would have been missed.

Lastly, we note that, in general, the oxides have lower lattice thermal conductivity than the reference carbides and nitrides that have lighter mass anions and greater

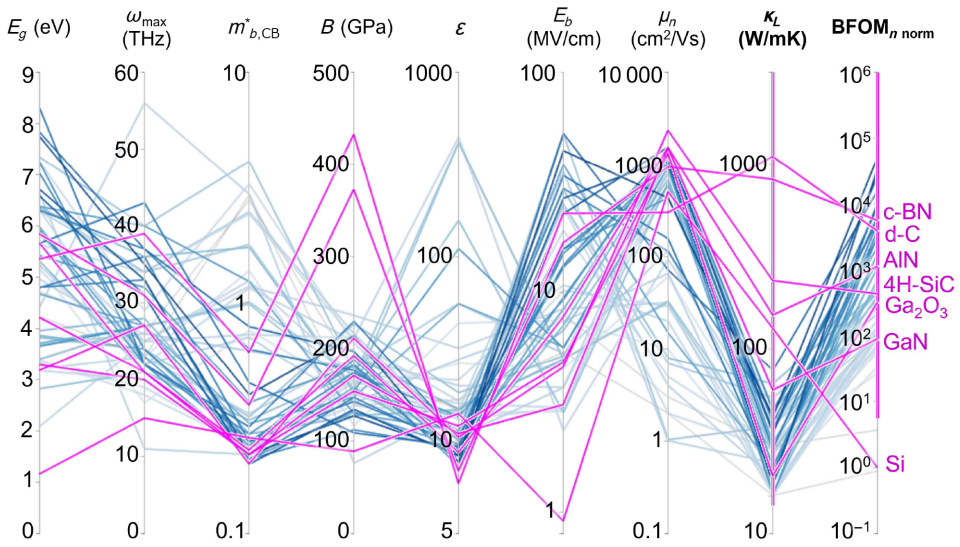

FIG. 5. Parallel coordinate plot of calculated electronic properties from HSE06 for all oxide candidates and the resultant n-type Baliga figures of merit. Magenta lines represent the reference power electronic materials. Blue lines represent all those candidates that fulfill the cutoff criteria for top candidates: $\kappa_L = 16$ W/mK and HSE06 BFOM$_{n-\text{norm}} = 10$. The blue color gradient is based upon BFOM$_{n-\text{norm}}$. Refer also to Tables S-III and S-IV within the Supplemental Material [7].

bulk moduli. This is a trade-off we must consider in elevated temperature applications where oxide chemistries are preferred.

IV. n-TYPE DOPABILITY ASSESSMENT

A. Qualitative ranking

Any material used as a conducting channel in power electronics must be able to be extrinsically doped to desired carrier concentrations. As a qualitative ranking of n-type dopability, the HSE06 electronic band edges of the remaining 47 candidates are shown in Fig. 6 aligned by their branch point energies. The dotted line represents E_{BP} using $N_{VB} = N_e/4$ and $N_{CB} = N_e/8$ and results from using other $N_{VB} : N_{CB}$ ratios are contained within the error bars.

The ranking also includes known n-type, ambipolar, p-type, and insulating ionic materials to gauge the method effectiveness and inform choice of the cutoff value. Only ionic bonded materials are used since the branch point energy calculation assumes that there is asymmetry in the number of valence and conduction bands. The n-type dopable reference materials are defined as having 10^{18}–10^{21} cm^{-3} electron carrier concentrations. Lightly n-type dopable materials are those that can achieve 10^{16}–10^{18} cm^{-3} carrier concentrations. Although some materials, like MgO, show activated transport after doping [66], we do not consider these materials dopable since we care only about electrons (holes) living inside or close to the conduction (valence) band. References for dopability status and carrier concentration can be found in Table S-VI within the Supplemental Material [7]. The materials have been arranged (left to right) by increasing distance of E_{BP} from the conduction-band minimum (CBM), scaled by their HSE06 band gaps.

As a rough assessment of accuracy, we compare our computed E_{BP} to experimental data from Ref. [57], as indicated by the bright green squares in Fig. 6. The experimental values are within our error bars for three of the four materials.

Materials on the left-hand side of Fig. 6 have computed E_{BP} inside or very close to the conduction band. This includes the reference n-type materials of wurtzite ZnO, SnO_2, In_2O_3, spinel Ga_2ZnO_4, and β-Ga_2O_3, as well as two top candidates $ZnSnO_3$ and $GaInO_3$, which can all reach 10^{19}–10^{20} cm^{-3} electron concentrations [14,22,67,68]. There are also materials that have been doped ambipolar in experiments (wurtzite GaN [22]) or are predicted ambipolar with defect calculations (rocksalt ZnO [13]).

Besides known power semiconductors (GaN and β-Ga_2O_3), only SnO_2, $ZnSnO_3$, and $GaInO_3$ have large enough Baliga figures of merit and κ_L to be considered top candidates among known n-type dopable materials (see Table S-VI within the Supplemental Material [7]). However, SnO_2 is not a WBG material and the measured single-crystal mobility [69] is smaller than predicted by our model (see Table S-II within the Supplemental Material [7]). Thus, SnO_2 is not presently considered for power devices. The trigonal $ZnSnO_3$ and $GaInO_3$ have been researched previously as transparent conducting n-type oxides, but their potential in power electronics has yet to be explored and thus will be discussed later [68,70].

As the E_{BP} moves toward the midgap, p-type and insulating materials begin to appear. This includes exclusively p-type materials like Cu_2O [22], $AlScO_3$ [71], and AlN

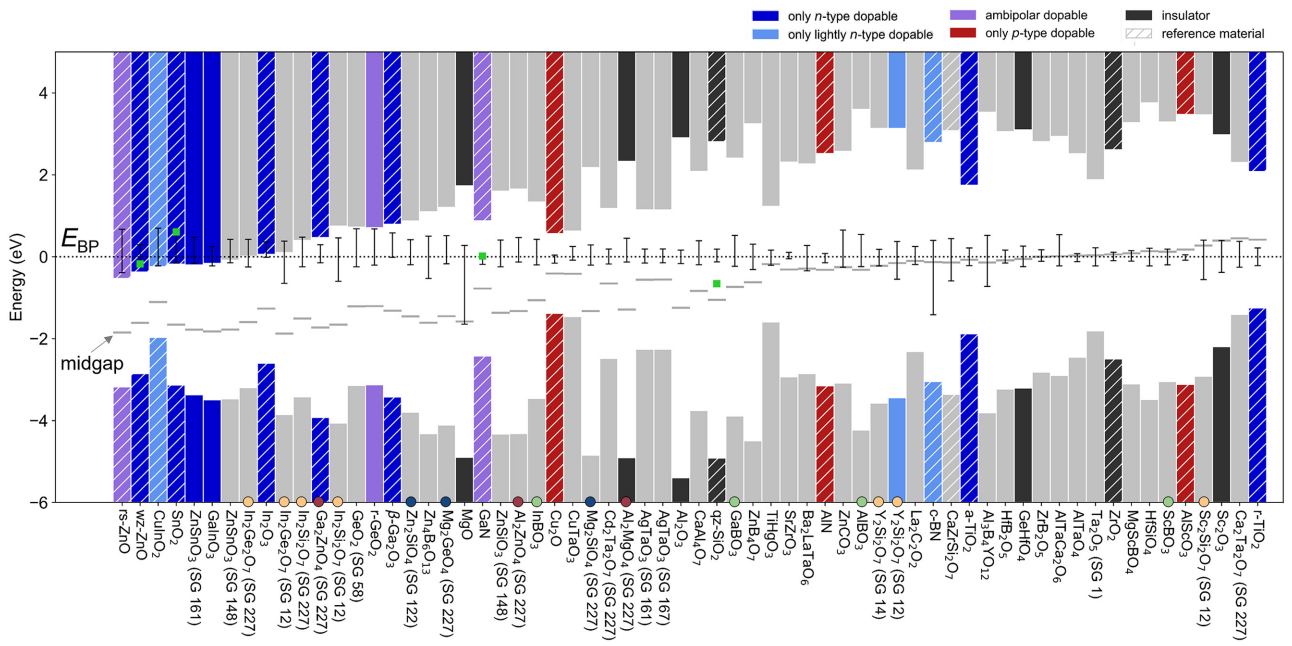

FIG. 6. HSE06 electronic bands of 47 top candidates and reference materials aligned by the branch point energy (E_{BP}) as indicated by the dotted line. Materials are arranged in ascending order of E_{BP} distance from the conduction-band edge scaled relative to the band gap. Calculations are performed with $N_{VB} = N_e/4$ and $N_{CB} = N_e/8$. Error bars represent the E_{BP} computed using different $N_{VB} : N_{CB}$ ratios. Bright green squares indicate experimental E_{BP} gathered from Shapera and Schleife [57]. Materials for which dopability is known are colored accordingly (see Table S-VI within the Supplemental Material [7]). Members of the families highlighted in this work are identified with colored circles.

that is considered *p* type here since highest electron concentrations have only reached 10^{15} cm^{-3} [72,73]. Insulators include quartz SiO_2 and ZrO_2 as well as five of our top candidates: MgO, spinel Al_2MgO_4, corundum Al_2O_3, Sc_2O_3, and the recently calculated $GeHfO_4$ [18]. The ranking, however, is not perfect. There are lightly *n*-type dopable materials like cubic BN and recently calculated $Y_2Si_2O_7$ [18]. In addition, both rutile and anatase versions of TiO_2 have E_{BP} near the midgap, even though they are known to be *n*-type dopable. The appearance of TiO_2 as a false negative was also discussed in Woods-Robinson *et al.* [56] and can likely be attributed to the appearance of Ti *d* orbitals at the bottom of the conduction band. Overall, the branch point energy ranking approach works well as a quick way to prioritize which materials might be more likely *n*-type dopable, although a few materials may be missed.

Looking at the top candidates more closely, we see common chemistries and stoichiometries emerge, creating "families" of materials. Among the highest-ranked compounds in Fig. 6 is a family of $(III)_2(IV)_2O_7$ compounds with thortveitite and pyrochlore polymorphs that are indicated by yellow dots in Figs. 4 and 6. Next we see the appearance of $(III)_2(II)O_4$ (red dot) and $(II)_2(IV)O_4$ (blue dot) compounds, many of which have a normal spinel crystal structure. The $(III)_2(II)O_4$ spinels are a known category of WBG materials that have already been explored for use in electronics, while the $(II)_2(IV)O_4$ compounds have not. Lastly, there are four $(III)BO_3$ borates with calcite crystal structure [space group (SG) number 167]. These do not rank as highly in the *n*-type dopability analysis as the other families but have incredible Baliga figures of merit, as shown by the green dots in Fig. 4.

For downselection at this stage, we consider Cu_2O as the cutoff point since all reference materials to the left in Fig. 6 allow *n*-type doping (besides MgO which has a large E_{BP} error bar). We are able to downselect from 47 to 14 candidates that were not previously considered for power electronics. The HSE06-calculated electronic properties of these 14 materials are shown in Table I. Many of these 14 most promising candidates are also members of the identified families.

B. Defect formation energy calculations

To add more confidence to the qualitative *n*-type dopability ranking, defect formation energy calculations are performed on two structures: high-ranking $In_2Ge_2O_7$ (SG 227), and low-ranking $CaZrSi_2O_7$. Native acceptor defects with low formation energy can accept electrons and, if present in large numbers, will compensate any dopant electrons, limiting the achievable free carrier concentration. Ideally, one would like acceptor defect formation energies

TABLE I. Computed electronic structure properties from HSE06 calculations of the top 14 previously unexplored *n*-type power electronic candidates. These candidates pass the *n*-type BFOM and κ_L criteria and are in the top half of the qualitative *n*-type dopability ranking. Shown here are the international space group number (SG Number), band gap (E_g), band effective mass for electrons ($m^*_{b,\mathrm{CB}}$), mobility of electrons (μ_n), breakdown field (E_b), dielectric constant (ε), *n*-type Baliga figure of merit, lattice thermal conductivity (κ_L), and nominal difference in energy between the conduction-band minimum (CBM) and branch point energy calculated with $N_{\mathrm{VB}} = N_e/4$ and $N_{\mathrm{CB}} = N_e/8$. The Baliga FOM has been normalized to the calculated *n*-type silicon HSE06 BFOM. Candidates are listed in alphabetical order. For more calculated compounds, see Table S-III within the Supplemental Material [7].

Compound	SG Number	E_g (eV)	$m^*_{b,\mathrm{CB}}$ (m_e)	μ_n ($\mathrm{cm^2/Vs}$)	E_b (MV/cm)	ε	$\mathrm{BFOM}_{n-\mathrm{norm}}$	κ_L (W/mK)	$E_{\mathrm{BP}} - \mathrm{CBM}$ (eV)
Al_2ZnO_4	227	6.0	0.24	1284	9.5	9	1790	19	−1.65
GeO_2	58	3.9	0.23	1513	5.0	15	507	46	−0.72
$GaInO_3$	194	3.3	0.24	1235	3.0	13	78	16	0.16
$In_2Ge_2O_7$	227	3.2	0.33	616	3.7	20	114	27	−0.01
$In_2Ge_2O_7$	12	4.0	0.27	691	6.7	15	572	31	−0.10
$In_2Si_2O_7$	227	3.8	0.32	811	5.1	18	367	40	−0.40
$In_2Si_2O_7$	12	4.8	0.21	1391	13.3	9	5503	40	−0.75
$InBO_3$	167	4.8	0.25	959	15.7	10	6570	29	−1.34
Mg_2GeO_4	227	5.3	0.23	1293	7.1	9	737	17	−1.21
Zn_2SiO_4	122	4.7	0.21	1335	8.4	9	1342	31	−0.88
$ZnSiO_3$	148	5.9	0.22	1514	9.3	14	3008	47	−1.60
$ZnSnO_3$	148	3.4	0.24	953	2.9	14	59	22	0.08
$ZnSnO_3$	161	3.2	0.23	1269	3.0	16	99	31	0.20
$Zn_4B_6O_{13}$	217	5.4	0.37	435	15.7	7	2249	37	−1.10

to become negative at a Fermi level that is inside the conduction band as this will allow dopants to increase the net electron concentration without spontaneous formation of compensating defects [74]. Figure 7 shows the formation energies calculated using the GGA+U method for all possible vacancy (V_A), interstitial (A_i), and antisite (A_B) point defects for each element (A) in $In_2Ge_2O_7$ (SG 227) and $CaZrSi_2O_7$. The x axis is the Fermi energy in electronvolts referenced from valence-band maximum to conduction-band minimum and represents the corrected band gap as calculated using the *GW* method.

The germanium-rich condition is the most favorable environment for *n*-type doping in pyrochlore $In_2Ge_2O_7$, as shown in Fig. 7(a). Under these conditions, the lowest-energy compensating defect, Ge_{In} with −1 charge state, will spontaneously form at a Fermi energy that is approximately 1 eV into the conduction band. In addition, this structure is predicted to be self-doped due to the low formation energy of oxygen vacancies that can act as shallow donors. This means that pyrochlore $In_2Ge_2O_7$ is likely intrinsically *n* type and there is room for increasing the electron concentration through extrinsic doping.

The opposite case is shown in Fig. 7(b). $CaZrSi_2O_7$ is insulating even in oxygen-poor conditions where *n*-type doping is most favorable. If donor dopants are added to $CaZrSi_2O_7$, the additional electrons will be compensated by native acceptor defects (i.e., Ca_{Zr}, V_{Ca}) pinning the Fermi energy at approximately 1.2 eV below the conduction-band minimum. These defect formation energy results confirm the predictions of the qualitative dopability ranking and further support pyrochlore $In_2Ge_2O_7$ as one of the most promising among the top power electronics candidates from our search.

V. DISCUSSION: SYNTHESIS OF TOP CANDIDATES

Another important factor for commercialization of semiconductors is the ability to synthesize as single crystals and/or thin films. Understanding whether and how the candidates have been historically grown will help experimental investigations. It should be noted that the absence of synthesis in the literature does not preclude a material from being realized in the future, but the available growth information allows prioritization of further studies.

Specifically, materials that can be easily grown as single crystals (e.g., Si, β-Ga_2O_3) allow melt-based bulk processing of substrate wafers that are then used to grow homoepitaxial thin films of the same material [20]. In the epitaxial growth method, new crystal layers are formed with desired orientation governed by the underlying substrate lattice. Doped native substrates are required for fabrication of vertical devices like those made with SiC, and are thus preferred for high-power applications. Alternatively, one can grow heteroepitaxially on non-native substrates that are closely lattice matched to the semiconductor. Heterostructures are used in the creation of lateral devices (e.g., GaN on Si). Lateral devices are less suited to high-power application, but are useful in the early stages of lab testing to make high-quality measurements of a material's electrical properties. Thus, we are interested in assessing both the single-crystal growth and availability of closely matched

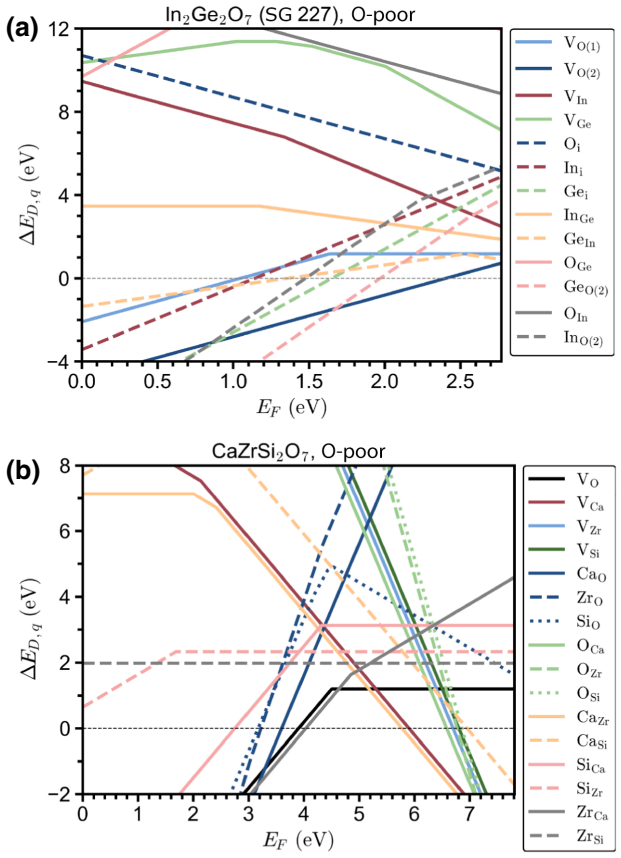

FIG. 7. Formation energies of native vacancy, interstitial, and antisite defects calculated using the supercell approach explained in Sec. II B 3. The Fermi energy is referenced from the valence-band maximum and plotted to the conduction-band minimum. Subscripts (1) and (2) indicate different Wycoff sites. (a) Pyrochlore $In_2Ge_2O_7$ is predicted to be *n*-type dopable under Ge-rich conditions. (b) $CaZrSi_2O_7$ is predicted to be *n*-type insulating even in favorable O-poor conditions.

non-native substrates for our top candidates. To address this synthesis and device integration potential, we consider the growth of the aforementioned novel families of materials: $(III)_2(IV)_2O_7$, $(III/II)_2(II/IV)_2O_4$, and $(III)BO_3$. Considering synthesis for material groups is useful since many compounds in the same family will share growth recipes and have similar material behaviors.

We analyze the available literature for each family to answer a few pertinent questions. (1) Has the material been synthesized and does it remain stable at ambient conditions? (2) Has the material been grown as a single crystal? (3) Is there demonstrated electrical conductivity or successful extrinsic doping? (4) Could the material be grown heteroepitaxially with a suitable substrate?

A. $(III)_2(IV)_2O_7$ family

The first family among top candidates is a group of 2-2-7 stoichiometry oxides of the form $(III)_2(IV)_2O_7$ where the group-III elements include In, Sc, or Y, and group-IV elements are Si or Ge. The In and Sc versions of this chemistry appear in two polymorphs: a ground-state thortveitite structure (SG 12) and a higher-pressure pyrochlore structure (SG 227). With its larger atomic radii, the yttrium versions have a different set of polymorphs. $Y_2Si_2O_7$ appears as thortveitite ground-state and several higher-temperature monoclinic and orthorhombic polymorphs [75]. Yttrium germanate's ground state is space group 96. According to the literature, a pyrochlore $Y_2Ge_2O_7$ [76,77] and several $Sc_2Ge_2O_7$ polymorphs have been synthesized in experiments [76,78,79], but none of these chemistries are included in the ICSD and are therefore not in this study. Of the ten ICSD structures in the $(III)_2(IV)_2O_7$ family, seven are top candidates for power electronics (see Fig. 4). In addition, the In versions of both the thortveitite and the pyrochlore structure rank within the upper half of our *n*-type dopability assessment (see Fig. 6). Native defect formation energy calculations completed in this work for pyrochlore $In_2Ge_2O_7$ further indicate that materials in this family may allow *n*-type doping [Fig. 7(a)].

Powders of the thortveitites have been synthesized using conventional solid-state reactions at elevated temperatures (1000–1500 °C) [76,78–81]. The pyrochlores can be stabilized in powder form using high pressure: 5.3 GPa for pyrogermanates and 12 GPa for pyrosilicates [78,80,81]. The thortveitite $In_2Si_2O_7$ has also been grown as single crystals of a few mm^2 and 1 mm thick using a flux method and $Li_2Mo_2O_7$ solvent [82]. Previous research into these materials focuses on fluoresence centers, catalysts, oxide fuel cells, and exotic behaviors like superconductivity, but not power electronics [78,80].

While our calculations show that $In_2Ge_2O_7$ pyrochlore is likely *n*-type dopable, its metastable state and high-pressure synthesis may make bulk growth difficult. In contrast, the thortveitite structure has potential for better high-power performance (see Table I), ranks in the top half of Fig. 6, and could be stably grown in bulk as a single crystal. This makes the thortveitite $In_2Ge_2O_7$ and $In_2Si_2O_7$ attractive candidates for power devices.

In order to synthesize the pyrochlore versions, we need to consider heteroepitaxial growth of thin films. Figure 8 shows the HSE06 relaxed lattice constant *a* of the pyrochlores along with a few common substrates: rutile TiO_2 and cubic yttria-stabilized zirconia (YSZ). Since the substrates are tetragonal and cubic, respectively, the *a* and *b* parameters are equivalent and separated by a right angle, just as in the pyrochlore structure. The lattice mismatch between the semiconductor and these two substrates is between 2% and 6%, which is within the acceptable tolerance. Figure 9 shows a schematic of the $In_2Ge_2O_7$ crystal on both substrates, displaying the close alignment at the (001) interface of the In/Ge cations with Ti or Zr that is necessary for successful epitaxial growth without significant interfacial strain. Given their indication of *n*-type

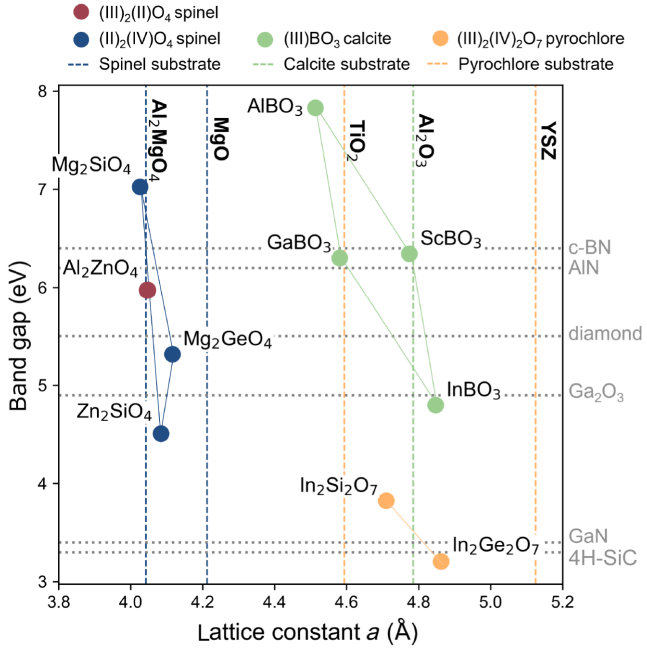

FIG. 8. Power electronic candidates from the three promising families: $(III)_2(IV)_2O_7$ pyrochlore, $(III/II)_2(II/IV)O_4$ normal spinels, and $(III)BO_3$ calcite. HSE06 calculated band gaps of candidates shown in comparison to experimental band gaps of known power electronic semiconductors. HSE06 calculated "*a*" lattice constant of candidates shown in comparison to experimental "*a*" lattice constants of potential substrates (color matched) for heteroepitaxial growth on the (001) surface. Half lattice constant shown for Al_2MgO_4 substrate, $(II)_2(IV)O_4$ spinels, and $(III)_2(IV)_2O_7$ pyrochlores.

dopability according to calculations and potential for heteroepitaxy, the pyrochlore 2-2-7 materials also have potential for power applications along with their ground-state versions.

B. $(III/II)_2(II/IV)O_4$ family

The next family of materials is 2-1-4 oxides. Within this stoichiometry, there are well-known spinels (SG 227) of chemistry $(III)_2(II)O_4$ where group-III elements are Al, Ga, In and group-II elements are Mg, Zn, Cd. There are also $(II)_2(IV)O_4$ compounds where group-II elements are Mg, Zn, Cd, and group-IV elements are Si, Ge, Sn. Several of the $(II)_2(IV)O_4$ compounds also take the spinel structure. All of the spinels calculated here are of the "normal" structure where the divalent B atoms of A_2BO_4 sit on the eight tetrahedral sites and the trivalent A atoms sit on the 16 octahedral sites. There also exist "inverse" spinels where a 100% inverted structure has all B atoms and half of A atoms occupy octahedral sites and the rest of A atoms occupy tetrahedral sites. Compounds like Ga_2MgO_4, Zn_2SnO_4, In_2MgO_4, Mg_2SnO_4, Al_2CdO_4 tend to form inverse spinels [83–87]. Since they are disordered, any experimentally known inverse spinel is omitted from our calculations for this family. Generally, the materials in this family have lower predicted lattice thermal conductivity and Baliga figure of merit than the other two identified families, but there are still quite a few that appear as top performers (see Fig. 4).

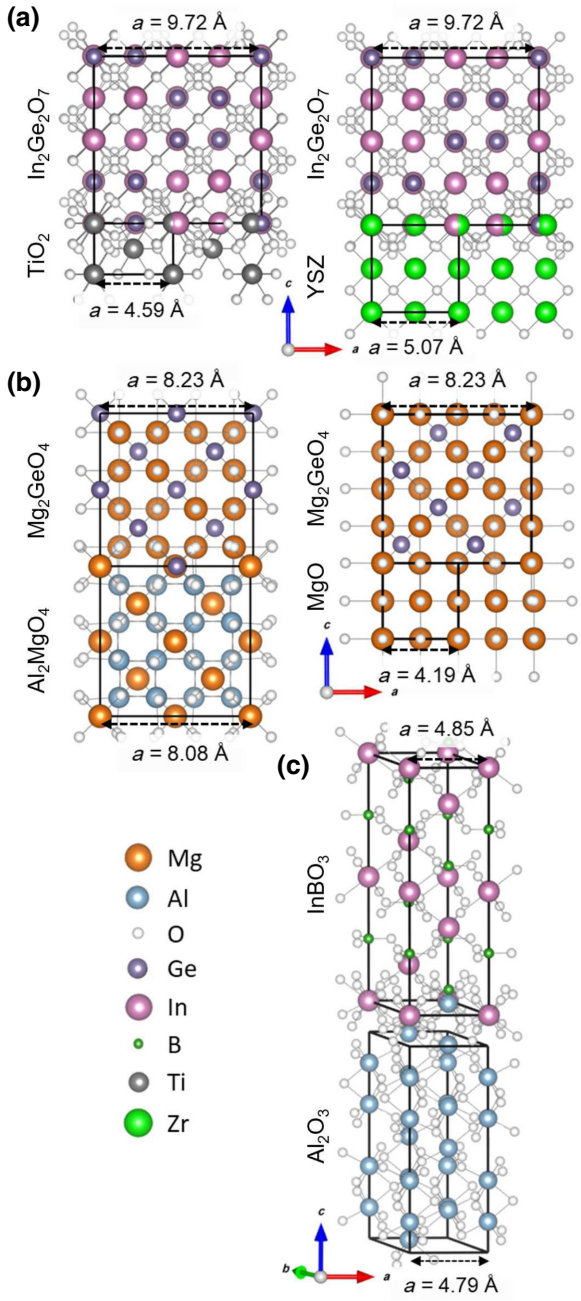

FIG. 9. Lattice matching of (001) surfaces for representatives from the three promising families with potential substrates: (a) $In_2Ge_2O_7$ pyrochlore (SG 227) on TiO_2 (SG 136) and yttria-stabilized ZrO_2 (SG 225), (b) Mg_2GeO_4 spinel (SG 227) on Al_2MgO_4 (SG 227) and MgO (SG 225), and (c) $InBO_3$ (SG 167) on Al_2O_3 (SG 167).

Let us first consider the $(III)_2(II)O_4$ compounds, also referred to as III-II spinels. Those compounds containing Ga or Al and Mg or Zn are higher performers than their In and Cd counterparts due to larger band gaps. Most of these compounds have been synthesized and are stable at ambient conditions. A few of these materials are of particular interest. Ga_2ZnO_4 is a known *n*-type single-crystal semiconductor as discussed previously [14,88,89]. According to our calculations, it has high Baliga FOM but low κ_L and is therefore not a top candidate. Al_2MgO_4 is a top candidate in our search but is a known insulator used as a single-crystal substrate for semiconductor devices.

The other top candidate from the III-II spinel family is Al_2ZnO_4. It has high Baliga FOM, decent κ_L, and is ranked in the upper half of our *n*-type dopability assessment. Powder samples of stoichiometric, normal Al_2ZnO_4 have been synthesized, but there are no accounts of single-crystal growth, electrical conductivity measurements, or attempts to dope this material [90]. With further investigation, this spinel compound may be *n*-type dopable like its gallium counterpart.

The $(II)_2(IV)O_4$ compounds have not been considered for power electronics to our knowledge. Like the traditional III-II materials, many of these II-IV versions form in the spinel structure. Depending on the ion species, pressure, and temperature, these compounds can also form in the inverse spinel, phenacite or willemite (SG 148), olivine (SG 64), modified-spinel or β (SG 74), and other lower symmetry polymorphs. The tin- and cadmium-containing compounds have low thermal conductivity and small band gaps (GGA+U $E_g < 2$ eV) and are thus not of interest for high-power electronics.

One top power electronic candidate from the II-IV compounds is Mg_2GeO_4 spinel. Polycrystals have been synthesized from the olivine ground-state structure by heating to 850 °C in a pressure vessel at 0.5 GPa. Once synthesized, the spinel is stable at ambient conditions, transitioning back to olivine above 810 °C [91,92]. There is also evidence that this material is intrinsically conductive due to the formation of native donor defects [93]. The measured conductivity of above 100 S/cm is larger than that of intrinsic Si, making this an appealing candidate for power electronics.

The next two candidates with high Baliga FOM and κ_L from this group are spinel Mg_2SiO_4 and trigonal Zn_2SiO_4. Although the germanate compounds often require less extreme temperature and pressure conditions to form, the silicate analogues have larger band gaps and thus higher Baliga figures of merit, as evidenced in Fig. 4. Like its germanium counterpart, Mg_2SiO_4 normal spinel is synthesized from the olivine ground state with an elevated temperature of 1200 °C and pressure of 22 GPa [94]. Once quenched, the spinel is stable up to about 700 °C. In our qualitative *n*-type dopabilty analysis, Mg_2SiO_4 is below our cutoff. In addition, previously published *ab initio* defect calculations indicate that none of the Mg_2SiO_4 polymorphs are likely *n*-type dopable [95]. The calculations of the olivine structure showed that Mg vacancies and O interstitials will likely compensate any addition electrons from extrinsic dopants. While the study did not conclusively test all possible conditions or defects for the spinel structure, these preliminary results make spinel Mg_2SiO_4 a less attractive candidate.

Of all the compounds in the II-IV group, zinc silicate has the most realized stable polymorphs. Select polymorphs are shown in Fig. 4. The trigonal (SG 122) polymorph is the only Zn_2SiO_4 with a large enough predicted κ_L to be included in the top candidate list. It is the second-lowest-energy polymorph with a wide range of stability. It can be formed from the ground-state "willemite" at 800 °C and 3–8 GPa [96]. The trigonal version also ranks above the cutoff in our *n*-type dopability analysis (see Fig. 6), which makes it an attractive candidate. To our knowledge, no one has attempted to dope any of the polymorphs of Zn_2SiO_4. Just below our chosen κ_L cutoff are two other zinc silicate polymorphs. The willemite structure (SG 148) has been grown as a single crystal of 10-mm^2 size in previous photoluminescence studies [97]. The spinel version is just below our top candidate cutoff but, unfortunately, was deemed the rarest and least stable polymorph according to theoretical calculations [98]. In addition, the ICSD entry for this normal spinel compound is based on theoretical calculations [99] and experimental entries all include some degree of inversion.

Lastly, the HSE06 calculated *a* lattice constants of the four previously unexplored top candidate spinels from this family are all within 2% of the Al_2MgO_4 substrate *a* lattice constant, as shown in Fig. 8, indicating that epitaxial growth on common substrates is possible. As seen in Fig. 9, the Mg cations of the Mg_2GeO_4 are near perfectly aligned to the Al cations of the (001) substrate since they are exactly the same space group. As an alternative, cubic MgO is equally well matched to the Mg cations at the corners and center of the unit cell at the interface.

If spinel Al_2ZnO_4 proves *n*-type dopable like some of its other family members, it could be a great power electronic candidate. Mg_2GeO_4 is also promising considering evidence of intrinsic *n*-type conductivity. Additionally, given the demonstrated single-crystal growth of the willemite Zn_2SiO_4, its higher-energy trigonal polymorph may be a good power electronic candidate as well.

C. $(III)BO_3$ family

The last group contains four borates that have $(III)BO_3$ stoichiometry and calcite structure (SG 167). Stable polycrystals of all four compounds have been grown. $AlBO_3$ requires hydrothermal high-pressure synthesis techniques [100] since it does not lie on the convex hull, but once synthesized, remains stable. In addition, single crystals of

$InBO_3$, $ScBO_3$, and $GaBO_3$ have been grown via molten flux at ambient pressures with the $GaBO_3$ crystals measuring $4 \times 4 \times 0.2$ mm^3 [100,101]. Despite this easy synthesis, to our knowledge no one has attempted to dope these materials or research them for power electronic applications. According to our analysis, these borates rank the lowest for *n*-type dopability potential (see Fig. 6) among the families. $InBO_3$ sits just above *p*-type Cu_2O and is the most promising for potential doping of the four. The calcite family has been studied mostly in the pursuit of rare-earth-doped phosphors for photoluminescence applications.

In addition to potential for native substrate growth, there are commercial substrates available for epitaxial growth of heterostructures. The cations of (001) $ScBO_3$ and $InBO_3$ match with the Al atoms at the (001) surface of Al_2O_3 (same space group 167) within 1.5%, as shown in Figs. 8 and 9. Given the very high figures of merit, demonstrated single-crystal growth, and potential heteroepitaxial growth, calcites in the $(III)BO_3$ family could make excellent candidates for power electronics.

D. Other candidates

There are also a handful of candidate oxides with large Baliga figures of merit, adequate κ_L, and E_{BP} close to the CBM that are not part of the families. These deserve to be considered for power electronics as well. We investigate the literature to evaluate the synthesis potential of the remaining candidates in Table I.

To start, the ground-state version of $ZnSnO_3$ (SG 161) and $GaInO_3$ have been grown as transparent conducting oxide thin films via dc sputtering and are self-doped through off-stoichiometry with room-temperature carrier concentrations around 10^{20} cm^{-3} [68,70]. Within the top candidates is also a higher-pressure polymorph of $ZnSnO_3$, which is less thermodynamically stable and has been synthesized only through low-temperature ion exchange [102]. To our knowledge, none of these materials have been considered for power electronics. Since they are unintentionally doped during synthesis, the question remains whether carrier concentrations can be controlled within the desired range for power electronics: 10^{16}–10^{20} cm^{-3}. In addition, these three compounds have HSE06 $BFOM_{n-norm}$ near or lower than GaN. While attractive for their dopability and evidence of thin-film synthesis, these compounds may not provide enough improvement in high-power performance to justify further exploration.

Upon further inspection, GeO_2 in space group 58 is a high-pressure polymorph of rutile (SG 136) with very similar properties. The rutile polymorph has already been proposed as a promising WBG semiconductor [10,103]. Attempts to synthesize thin films of rutile GeO_2 have been difficult due to the existence of competing amorphous and quartz phases [11] and high vapor pressure [12], making our high-pressure polymorph a less attractive candidate for further exploration.

$ZnSiO_3$ (SG 148) comes from an ICSD entry based upon a theoretical structure rather than experimental. At 140 meV above the convex hull, this is an unstable polymorph that easily decomposes into SiO_2 and the ground-state Zn_2SiO_4 [98].

The cubic metaborate $Zn_4B_6O_{13}$ lies on the convex hull. Bulk single crystals of optical quality have been grown by melt methods, making this attractive for further exploration [104]. It has been doped with rare-earth elements for luminescence applications [105,106], but has yet to be explored as a power semiconductor.

VI. CONCLUSION

Using a multistage first-principles computational workflow, we conducted a search among binary, ternary, and quaternary oxides for promising wide-band-gap *n*-type semiconductors for high-power, high-voltage, and high-temperature performance. We used a high-throughput evaluation of the Baliga figure of merit and thermal conductivity to downselect candidates based upon theoretical performance followed by a more detailed analysis of the electronic structure, *n*-type dopability, and prior synthesis of select candidates. Through the use of DFT and updated phenomenological models, we uphold the expected trends in theoretical performance of currently used or investigated power electronic materials such as Si, GaN, SiC, and β-Ga_2O_3. Out of the 1340 oxides considered, we identified 47 novel promising candidates, most of which are ternaries, that rival the high-power and high-voltage performance of GaN and 4H-SiC, and the lattice thermal conductivity of β-Ga_2O_3. We also highlight 14 compounds that are most likely to be *n*-type dopable according to our ranking of the branch point energy.

Of these top materials, many fall into three previously unexplored families of ternary compounds: $(III)_2(IV)_2O_7$, $(II)_2(IV)O_4$, and $(III)BO_3$. The $(III)_2(IV)_2O_7$ family contains germanates and silicates that adopt stable thortveitite (SG 12) and metastable pyrochlore (SG 227) structures. The thortveitite versions have been grown as single crystals, opening the opportunity for growth of bulk native substrates via large-scale processes. The more symmetric pyrochlore structures will be more difficult to synthesize in bulk, but thin films could be grown heteroepitaxially on common substrates, reducing the required synthesis temperatures and pressures. The indium-containing members of this family rank high in our qualitative *n*-type dopability analysis. Defect formation energy calculations on pyrochlore $In_2Ge_2O_7$ confirm that it has the potential to be intrinsically *n* type and accomodate further extrinsic dopants without worry of compensation by native acceptor defects.

The $(II)_2(IV)O_4$ family contains many polymorphs, the most interesting of which is the high-symmetry, stable spinel structure. From this set, Mg_2GeO_4 has exhibited evidence of intrinsic *n*-type conductivity, indicating that it could be easily doped to desired concentrations. In addition, heterostructures of several of these compounds could be grown epitaxially on Al_2MgO_4 or MgO substrates with acceptable lattice mismatch.

The $(III)BO_3$ calcite-structure borates have some of the largest predicted Baliga FOM values and have been grown as single crystals, indicating that they could be used as native substrates for vertical power devices. Alternatively, they could be grown heteroepitaxially on Al_2O_3 substrates. Of these, $InBO_3$ is the most promising candidate as it has the most potential to be *n*-type dopable according to our ranking.

While there is no evidence of melt growth for any of these candidates in the literature, that does not preclude them from future growth with this preferred industrial process, especially for those that lie on the convex hull and melt congruently. Therefore, we consider synthesis as a factor in prioritization of future work, but do not eliminate candidates based solely upon their historical growth conditions. Taking into consideration all of these relevant factors, we propose the strongest candidate from each of the identified families for future power electronics research: $In_2Ge_2O_7$ thortveitite and pyrochlore, Mg_2GeO_4 spinel, and $InBO_3$ calcite.

Future efforts must address the native defect formation energies of those high-ranked materials that were not confirmed in this study. In addition, suitable extrinsic dopants will need to be determined to realize the proposed materials' potential for power electronics. Once identified, experimental work can confirm these predictions through synthesis, epitaxial growth, and conductivity measurements. This includes a detailed analysis of whether it is feasible and affordable to make wafers using large-scale commercial processes. These identified wide-band-gap ternary oxides hold promise for future high-power, high-voltage, and high-temperature power electronics. We hope this work sparks deeper investigation into the potential of these materials to push the performance boundary of power electronics devices and aid in the renewable energy transition.

ACKNOWLEDGMENTS

This work was authored in part at the National Renewable Energy Laboratory (NREL) operated by Alliance for Sustainable Energy, LLC, for the U.S. Department of Energy (DOE) under Contract No. DE-AC36-08GO28308. Funding is provided by the Laboratory Directed Research and Development (LDRD) program at NREL and Advanced Energy Systems Graduate Program at the Colorado School of Mines. The research was performed using computational resources sponsored by the DOE's Office of Energy Efficiency and Renewable Energy located at NREL. The views expressed in the article do not necessarily represent the views of the DOE or the U.S. Government.

[1] R. J. Kaplar, J. C. Neely, D. L. Huber, and L. J. Rashkin, Generation-after-next power electronics: Ultrawide-bandgap devices, high-temperature packaging, and magnetic nanocomposite materials, IEEE Power Electron. Mag. **4**, 36 (2017). conference Name: IEEE Power Electronics Magazine

[2] S. M. Shinde, K. D. Patil, S. S. Khairnar, and W. Z. Gandhare, in *2009 Second International Conference on Emerging Trends in Engineering Technology* (2009), p. 726, iSSN: 2157-0485.

[3] A. Q. Huang, Power semiconductor devices for smart grid and renewable energy systems, Proc. IEEE 105, 2019 (2017). conference Name: Proceedings of the IEEE

[4] L. M. Tolbert, T. J. King, B. Ozpineci, J. Campbell, G. Muralidharan, D. Rizy, A. Sabau, H. Zhang, W. Zhang, Y. Xu, H. Huq, and H. Liu, Power electronic for distributed energy systems and transmission and distribution applications (2005).

[5] S. J. Pearton, F. Ren, M. Tadjer, and J. Kim, Perspective: Ga_2O_3 for ultra-high power rectifiers and MOSFETS, J. Appl. Phys. **124**, 220901 (2018).

[6] J. Y. Tsao, *et al.*, Ultrawide-bandgap semiconductors: Research opportunities and challenges, Adv. Electron. Mater. **4**, 1600501 (2018).

[7] A. Yuvaraj, See Supplemental Material at http://link.aps.org/supplemental/10.1103/PRXEnergy.1.033006 for HSE06 computed properties of the top candidates from this work, a comparison of GGA+U and HSE06 methods, and measured properties for reference materials, which includes Refs. [107–189].

[8] B. J. Baliga, Semiconductors for high-voltage, vertical channel field-effect transistors, J. Appl. Phys. **53**, 1759 (1982).

[9] K. Bushick, K. A. Mengle, S. Chae, and E. Kioupakis, Electron and hole mobility of rutile GeO_2 from first principles: An ultrawide-bandgap semiconductor for power electronics, Appl. Phys. Lett. **117**, 182104 (2020). publisher: American Institute of Physics

[10] S. Chae, J. Lee, K. A. Mengle, J. T. Heron, and E. Kioupakis, Rutile GeO_2: An ultrawide-band-gap semiconductor with ambipolar doping, Appl. Phys. Lett. **114**, 102104 (2019). publisher: American Institute of Physics

[11] S. Chae, H. Paik, N. M. Vu, E. Kioupakis, and J. T. Heron, Epitaxial stabilization of rutile germanium oxide thin film by molecular beam epitaxy, Appl. Phys. Lett. **117**, 072105 (2020). publisher: American Institute of Physics

[12] S. Chae, K. Mengle, K. Bushick, J. Lee, N. Sanders, Z. Deng, Z. Mi, P. F. P. Poudeu, H. Paik, J. T. Heron, and E. Kioupakis, Toward the predictive discovery of ambipolarly dopable ultra-wide-band-gap semiconductors: The case of rutile GeO2, Appl. Phys. Lett. **118**, 260501 (2021). publisher: American Institute of Physics

[13] A. Goyal and V. Stevanović, Metastable rocksalt ZnO is p-type dopable, Phys. Rev. Mater. **2**, 084603 (2018).

[14] Z. Galazka, S. Ganschow, R. Schewski, K. Irmscher, D. Klimm, A. Kwasniewski, M. Pietsch, A. Fiedler, I. Schulze-Jonack, M. Albrecht, T. Schröder, and M. Bickermann, Ultra-wide bandgap, conductive, high mobility, and high quality melt-grown bulk $ZnGa_2O_4$ single crystals, APL Mater. **7**, 022512 (2019). publisher: American Institute of Physics

[15] Z. Galazka, D. Klimm, K. Irmscher, R. Uecker, R. Schewski, and M. Bickermann, $MgGa_2O_4$ as a new wide bandgap transparent semiconducting oxide: Growth and properties of bulk single crystals, Phys. Status Solidi a **212**, 1455 (2015).

[16] A. Boonchun, K. Dabsamut, and W. R. L. Lambrecht, First-principles study of point defects in $LiGaO_2$, J. Appl. Phys. **126**, 155703 (2019). publisher: American Institute of Physics

[17] K. Dabsamut, A. Boonchun, and W. R. L. Lambrecht, First-principles study of n- and p-type doping opportunities in LiGaO2, J. Phys. D: Appl. Phys. **53**, 274002 (2020). publisher: IOP Publishing

[18] P. Gorai, R. W. McKinney, N. M. Haegel, A. Zakutayev, and V. Stevanovic, A computational survey of semiconductors for power electronics, Energy Environ. Sci. **12**, 3338 (2019).

[19] M. Hellenbrandt, The Inorganic Crystal Structure Database (ICSD)—Present and future, Crystallogr. Rev. **10**, 17 (2004).

[20] S. Reese, T. Remo, J. Green, and A. Zakutayev, How much will gallium oxide power electronics cost?, Joule **3**, 899 (2019).

[21] H. He, in *Solution Processed Metal Oxide Thin Films for Electronic Applications*, Metal Oxides, edited by Z. Cui and G. Korotcenkov (Elsevier, 2020), p. 7.

[22] A. Goyal, P. Gorai, S. Anand, E. S. Toberer, G. J. Snyder, and V. Stevanović, On the dopability of semiconductors and governing material properties, Chem. Mater. **32**, 4467 (2020).

[23] A. Schleife, F. Fuchs, C. Rödl, J. Furthmüller, and F. Bechstedt, Branch-point energies and band discontinuities of III-nitrides and III-/II-oxides from quasiparticle band-structure calculations, Appl. Phys. Lett. **94**, 012104 (2009). publisher: American Institute of Physics

[24] J. Robertson and S. J. Clark, Limits to doping in oxides, Phys. Rev. B **83**, 075205 (2011).

[25] J. Yan, P. Gorai, B. Ortiz, S. Miller, S. A. Barnett, T. Mason, V. Stevanović, and E. S. Toberer, Material descriptors for predicting thermoelectric performance, Energy Environ. Sci. **8**, 983 (2015).

[26] M. Lundstrom, Fundamentals of Carrier Transport, 2nd edn, Meas. Sci. Technol. **13**, 230 (2002).

[27] M. Cardona and P. Y. Yu, in *Fundamentals of Semiconductors* (Springer, Berlin, Heidelberg, 1996).

[28] P. Gorai, V. Stevanović, and E. S. Toberer, Computationally guided discovery of thermoelectric materials, Nat. Rev. Mater. **2**, 1 (2017).

[29] V. Stevanovic, P. Gorai, B. Ortiz, and E. S. Toberer, in *Computational Materials Discovery*, edited by A. R. Oganov, G. Saleh, and A. G. Kvashnin (Royal Society of Chemistry (RSC), 2019), p. 240.

[30] J. Zhang, L. Song, S. H. Pedersen, H. Yin, L. T. Hung, and B. B. Iversen, Discovery of high-performance low-cost n-type Mg_3Sb_2-based thermoelectric materials with multi-valley conduction bands, Nat. Commun. **8**, 13901 (2017).

[31] B. R. Ortiz, P. Gorai, L. Krishna, R. Mow, A. Lopez, R. McKinney, V. Stevanović, and E. S. Toberer, Potential for high thermoelectric performance in n-type Zintl compounds: A case study of Ba doped $KAlSb_4$, J. Mater. Chem. A **5**, 4036 (2017).

[32] P. Gorai, A. Ganose, A. Faghaninia, A. Jain, and V. Stevanović, Computational discovery of promising new n-type dopable ABX Zintl thermoelectric materials, Mater. Horiz. **7**, 1809 (2020).

[33] C. Kim, G. Pilania, and R. Ramprasad, From organized high-throughput data to phenomenological theory using machine learning: The example of dielectric breakdown, Chem. Mater. **28**, 1304 (2016).

[34] Y. Sun, S. A. Boggs, and R. Ramprasad, The intrinsic electrical breakdown strength of insulators from first principles, Appl. Phys. Lett. **101**, 132906 (2012). publisher: American Institute of Physics

[35] S. A. Miller, P. Gorai, B. R. Ortiz, A. Goyal, D. Gao, S. A. Barnett, T. O. Mason, G. J. Snyder, Q. Lv, V. Stevanović, and E. S. Toberer, Capturing anharmonicity in a lattice thermal conductivity model for high-throughput predictions, Chem. Mater. **29**, 2494 (2017).

[36] J. P. Perdew, K. Burke, and M. Ernzerhof, Generalized Gradient Approximation Made Simple, Phys. Rev. Lett. **77**, 3865 (1996).

[37] P. E. Blöchl, Projector augmented-wave method, Phys. Rev. B **50**, 17953 (1994).

[38] G. Kresse and J. Furthmüller, Efficient iterative schemes for ab initio total-energy calculations using a plane-wave basis set, Phys. Rev. B **54**, 11169 (1996).

[39] X. Zhang, V. Stevanović, M. d'Avezac, S. Lany, and A. Zunger, Prediction of A_2BX_4 metal-chalcogenide compounds via first-principles thermodynamics, Phys. Rev. B **86**, 014109 (2012).

[40] S. L. Dudarev, G. A. Botton, S. Y. Savrasov, C. J. Humphreys, and A. P. Sutton, Electron-energy-loss spectra and the structural stability of nickel oxide: An LSDA+U study, Phys. Rev. B **57**, 1505 (1998).

[41] V. Stevanović, S. Lany, X. Zhang, and A. Zunger, Correcting density functional theory for accurate predictions of compound enthalpies of formation: Fitted elemental-phase reference energies, Phys. Rev. B **85**, 115104 (2012).

[42] A. S. Barker and M. Ilegems, Infrared lattice vibrations and free-electron dispersion in GaN, Phys. Rev. B **7**, 743 (1973).

[43] M. Suzuki, T. Uenoyama, and A. Yanase, First-principles calculations of effective-mass parameters of AlN and GaN, Phys. Rev. B **52**, 8132 (1995).

[44] K. Kim, W. R. L. Lambrecht, B. Segall, and M. van Schilfgaarde, Effective masses and valence-band splittings in GaN and AlN, Phys. Rev. B **56**, 7363 (1997).

[45] B. Rheinländer and H. Neumann, Plasma Faraday rotation in n-type GaN, Phys. Status Solidi (b) **64**, K123 (1974).

[46] N. T. Son, W. M. Chen, O. Kordina, A. O. Konstantinov, B. Monemar, E. Janzén, D. M. Hofman, D. Volm,

M. Drechsler, and B. K. Meyer, Electron effective masses in 4H SiC, Appl. Phys. Lett. **66**, 1074 (1995).
[47] D. Volm, B. K. Meyer, D. M. Hofmann, W. M. Chen, N. T. Son, C. Persson, U. Lindefelt, O. Kordina, E. Sörman, A. O. Konstantinov, B. Monemar, and E. Janzén, Determination of the electron effective-mass tensor in 4 *H* SiC, Phys. Rev. B **53**, 15409 (1996).
[48] F. Birch, Finite elastic strain of cubic crystals, Phys. Rev. **71**, 809 (1947). publisher: American Physical Society
[49] F. D. Murnaghan, Finite deformations of an elastic solid, Am. J. Math. **59**, 235 (1937). publisher: Johns Hopkins University Press
[50] S. Baroni and R. Resta, Ab initio calculation of the macroscopic dielectric constant in silicon, Phys. Rev. B **33**, 7017 (1986). publisher: American Physical Society
[51] M. Gajdoš, K. Hummer, G. Kresse, J. Furthmüller, and F. Bechstedt, Linear optical properties in the projector-augmented wave methodology, Phys. Rev. B **73**, 045112 (2006). publisher: American Physical Society
[52] J. Heyd, G. E. Scuseria, and M. Ernzerhof, Hybrid functionals based on a screened Coulomb potential, J. Chem. Phys. **118**, 8207 (2003). publisher: American Institute of Physics
[53] J. Heyd, G. E. Scuseria, and M. Ernzerhof, Erratum: "Hybrid functionals based on a screened Coulomb potential" [J. Chem. Phys. 118, 8207 (2003)], J. Chem. Phys. **124**, 219906 (2006). publisher: American Institute of Physics
[54] M. Marsman, J. Paier, A. Stroppa, and G. Kresse, Hybrid functionals applied to extended systems, J. Phys.: Condens. Matter **20**, 064201 (2008). publisher: IOP Publishing
[55] A. Goyal, P. Gorai, H. Peng, S. Lany, and V. Stevanović, A computational framework for automation of point defect calculations, Comput. Mater. Sci. **130**, 1 (2017).
[56] R. Woods-Robinson, D. Broberg, A. Faghaninia, A. Jain, S. S. Dwaraknath, and K. A. Persson, Assessing high-throughput descriptors for prediction of transparent conductors, Chem. Mater. **30**, 8375 (2018).
[57] E. P. Shapera and A. Schleife, Database-driven materials selection for semiconductor heterojunction design, Adv. Theory Simul. **1**, 1800075 (2018).
[58] S. Lany and A. Zunger, Accurate prediction of defect properties in density functional supercell calculations, Modell. Simul. Mater. Sci. Eng. **17**, 084002 (2009). publisher: IOP Publishing
[59] M. Shishkin and G. Kresse, Self-consistent *GW* calculations for semiconductors and insulators, Phys. Rev. B **75**, 235102 (2007).
[60] J. Wang, H. Zhou, J. Zhang, Z. Liu, S. Xu, Q. Feng, J. Ning, C. Zhang, P. Ma, J. Zhang, and Y. Hao, Demonstration of $Al_{0.85}Ga0.15N$ Schottky barrier diode with > 3 kV breakdown voltage and the reverse leakage currents formation mechanism analysis, Appl. Phys. Lett. **118**, 173505 (2021).
[61] H. Ahmad, J. Lindemuth, Z. Engel, C. M. Matthews, T. M. McCrone, and W. A. Doolittle, Substantial P-type conductivity of AlN achieved via beryllium doping, Adv. Mater. **33**, 2104497 (2021).
[62] H. Ahmad, Z. Engel, C. M. Matthews, S. Lee, and W. A. Doolittle, Realization of homojunction PN AlN diodes, J. Appl. Phys. **131**, 175701 (2022).
[63] A. Allerman, A. Armstrong, A. Fischer, J. Dickerson, M. Crawford, M. King, M. Moseley, J. Wierer, and R. Kaplar, $Al_{0.3}Ga_{0.7}N$ PN diode with breakdown voltage > 1600 V, Electron. Lett. **52**, 1319 (2016).
[64] S. Pearton, ed., *GaN and ZnO-based Materials and Devices*, Springer Series in Materials Science, Vol. 156 (Springer Berlin Heidelberg, Berlin, Heidelberg, 2012).
[65] B. Sarkar, S. Washiyama, M. H. Breckenridge, A. Klump, J. N. Baker, P. Reddy, J. Tweedie, S. Mita, R. Kirste, D. L. Irving, R. Collazo, and Z. Sitar, N- and P- type Doping in Al-rich AlGaN and AlN, ECS Trans. **86**, 25 (2018).
[66] M. M. Tardío, R. Ramírez, R. González, and Y. Chen, *P* -type semiconducting properties in lithium-doped MgO single crystals, Phys. Rev. B **66**, 134202 (2002).
[67] J. M. Phillips, J. Kwo, G. A. Thomas, S. A. Carter, R. J. Cava, S. Y. Hou, J. J. Krajewski, J. H. Marshall, W. F. Peck, D. H. Rapkine, and R. B. van Dover, Transparent conducting thin films of GaInO3, Appl. Phys. Lett. **65**, 115 (1994).
[68] T. Minami, Transparent and conductive multicomponent oxide films prepared by magnetron sputtering, J. Vac. Sci. Technol. A **17**, 1765 (1999).
[69] C. G. Fonstad and R. H. Rediker, Electrical properties of high-quality stannic oxide crystals, J. Appl. Phys. **42**, 2911 (1971).
[70] T. Minami, H. Sonohara, S. Takata, and H. Sato, Highly transparent and conductive zinc-stannate thin films prepared by RF magnetron sputtering, Jpn. J. Appl. Phys. **33**, L1693 (1994).
[71] C.-W. Lee, P. Gorai, E. Garrity, A. Zakutayev, and V. Stevanović, AlScO3 perovskite—An ∼ 8 eV bandgap oxide predicted to exhibit low small hole polaron ionization energies and p-type conductivity at elevated temperatures, Appl. Phys. Lett. **121**, 102103 (2022).
[72] Y. Taniyasu and M. Kasu, Aluminum nitride deep-ultraviolet light-emitting p–n junction diodes, Diamond Relat. Mater. Proc. Diamond 2007, the 18th Eur. Conf. Diamond, Diamond-Like Mater., Carbon Nanotubes, Nitrides and Silicon Carbide **17**, 1273 (2008).
[73] Y. Taniyasu, M. Kasu, and T. Makimoto, Electrical conduction properties of n-type Si-doped AlN with high electron mobility (> 100 $cm^2V^{-1}s^{-1}$), Appl. Phys. Lett. **85**, 4672 (2004). publisher: American Institute of Physics
[74] A. Zunger, Practical doping principles, Appl. Phys. Lett. **83**, 57 (2003).
[75] J. Ito and H. Johnson, Synthesis and study of yttrialite, Am. Mineral. **53**, 1940 (1968).
[76] R. D. Shannon and A. W. Sleight, Synthesis of new high-pressure pyrochlore phases, Inorg. Chem. **7**, 1649 (1968).
[77] G. J. Redhammer, G. Roth, and G. Amthauer, Yttrium pyrogermanate, $Y_2Ge_2O_7$, Acta Crystallogr. Sect. C: Cryst. Struct. Commun. **63**, i93 (2007). number: 10 Publisher: International Union of Crystallography
[78] H. Li, S. Ma, Z. Yu, H. Zhu, and N. Li, In-situ high-pressure X-ray diffraction of the two polymorphs of $Sc_2Ge_2O_7$, AIP Adv. **10**, 00 (2020).

[79] R. Shannon and C. Prewitt, Synthesis of pyrosilicates and pyrogermanates having the thortveitite structure, J. Solid State Chem. **2**, 199 (1970).

[80] H. Li, Y. Li, N. Li, Y. Zhao, H. Zhu, P. Zhu, and X. Wang, A comparative study of high pressure behaviors of pyrochlore-type and thortveitite-type $In_2Ge_2O_7$, RSC Adv. **5**, 44121 (2015). publisher: The Royal Society of Chemistry

[81] A. F. Reid, C. Li, and A. E. Ringwood, High-pressure silicate pyrochlores, $Sc_2Si_2O_7$ and $In_2Si_2O_7$, J. Solid State Chem. **20**, 219 (1977).

[82] Y. Messous, B. Chambon, M. De Jésus, D. Drain, C. Pastor, A. Garcia, J. Chaminade, T. Gaewdang, C. Fouassier, B. Jacquier, and B. Varrel, Indium disilicate, a new fast scintillator, Nucl. Instrum. Methods Phys. Res. Sect. A: Accelerators, Spec., Detectors Associated Equipment **354**, 527 (1995).

[83] A. Kan, T. Moriyama, S. Takahashi, and H. Ogawa, Cation distributions and microwave dielectric properties of spinel-structured MgGa2o4ceramics, Jpn. J. Appl. Phys. **52**, 09KH01 (2013).

[84] K. Jeyadheepan and C. Sanjeeviraja, Preparation and crystal structures of some compounds: Powder X-ray diffraction and rietveld analysis, J. Chem. **2014**, e245918 (2014). publisher: Hindawi

[85] T. F. W. Barth and E. Posnjak, Spinel structures: with and without variate atom equipoints, Z. für Kristallogr. - Crystall. Mater. **82**, 325 (1932). publisher: Oldenbourg Wissenschaftsverlag

[86] P. Poix and A. Michel, Etude cristallographique et magnetique des orthostannates de magnesium, de zinc et de cobalt, BULLETIN DE LA SOCIETE CHIMIQUE DE FRANCE, 1653 (1959).

[87] H. Hahn, G. Frank, W. Klingler, A. D. Störger, and G. Störger, Untersuchungen über ternäre Chalkogenide. VI. Über Ternäre Chalkogenide des Aluminiums, Galliums und Indiums mit Zink, Cadmium und Quecksilber, Zeitschrift für Anorganische und Allgemeine Chemie **279**, 241 (1955).

[88] R.-H. Horng, C.-Y. Huang, S.-L. Ou, T.-K. Juang, and P.-L. Liu, Epitaxial growth of $ZnGa_2O_4$: A new, deep ultraviolet semiconductor candidate, Cryst. Growth Des. **17**, 6071 (2017). publisher: American Chemical Society

[89] E. Chikoidze, C. Sartel, I. Madaci, H. Mohamed, C. Vilar, B. Ballesteros, F. Belarre, E. del Corro, P. Vales-Castro, G. Sauthier, L. Li, M. Jennings, V. Sallet, Y. Dumont, and A. Pérez-Tomás, p-type ultrawide-band-gap spinel $ZnGa_2O_4$, new perspectives for energy electronics, Cryst. Growth Des. **20**, 2535 (2020).

[90] D. Levy, A. Pavese, A. Sani, and V. Pischedda, Structure and compressibility of synthetic $ZnAl_2O_4$ (gahnite) under high-pressure conditions, from synchrotron X-ray powder diffraction, Phys. Chem. Miner. **28**, 612 (2001). company: Springer Distributor: Springer Institution: Springer Label: Springer Number: 9 Publisher: Springer-Verlag

[91] A. Navrotsky, Thermodynamic relations among olivine, spinel, and phenacite structures in silicates and germanates: I. Volume relations and the systems NiO-MgO-GeO_2 and CoO-MgO-GeO_2, J. Solid State Chem. **6**, 21 (1973).

[92] R. B. Von Dreele, A. Navrotsky, and A. L. Bowman, Refinement of the crystal structure of Mg_2GeO_4 spinel, Acta Crystall. Sect. B: Struct. Crystall. Cryst. Chem. **33**, 2287 (1977). number: 7 Publisher: International Union of Crystallography

[93] A. Rehman, J. Jacob, R. Zahra, K. Mahmood, A. Ali, U. Rehaman, Y. Ali, A. Ashfaq, W. Ahmed, S. Ikram, N. Amin, and S. Hussain, Growth of Mg_2GeO_4 nano-crystals on Si substrate and modulation of Seebeck coefficient by post growth annealing technique, Ceram. Int. **45**, 16275 (2019).

[94] M. Akaogi, N. L. Ross, P. McMillan, and A. Navrotsky, The Mg_2SiO_4 polymorphs (olivine, modified spinel and spinel)–thermodynamic properties from oxide melt solution calorimetry, phase relations, and models of lattice vibrations, Am. Mineral. **69**, 499 (1984).

[95] A. K. Verma and B. B. Karki, Ab initio investigations of native and protonic point defects in Mg_2SiO_4 polymorphs under high pressure, Earth Planet Sci. Lett. **285**, 140 (2009).

[96] Y. Syono, S.-I. Akimoto, and Y. Matsui, High pressure transformations in zinc silicates, J. Solid State Chem. **3**, 369 (1971). publisher: Academic Press

[97] I. Chang, P. Thioulouse, E. Mendez, E. Giess, D. Dove, and T. Takamori, Photoexcited and photostimulated luminescence and conduction in zinc silicate single crystals with deep centers and traps, J. Lumin. **24-25**, 313 (1981).

[98] S. Z. Karazhanov, P. Ravindran, P. Vajeeston, A. G. Ulyashin, H. Fjellvag, and B. G. Svensson, Phase stability and pressure-induced structural transitions at zero temperature in $ZnSiO_3$ and Zn_2SiO_4, J. Phys.: Condens. Matter **21**, 485801 (2009). publisher: IOP Publishing

[99] D. Allali, A. Bouhemadou, E. M. A. A. Safi, S. Bin-Omran, M. Chegaar, R. Khenata, and A. H. Reshak, Electronic and optical properties of the SiB_2O_4 (B=Mg, Zn, and Cd) spinel oxides: An ab initio study with the Tran–Blaha-modified Becke–Johnson density functional, Phys. B: Condens. Matter **443**, 24 (2014).

[100] D. Santamaría-Pérez, O. Gomis, J. A. Sans, H. M. Ortiz, Á. Vegas, D. Errandonea, J. Ruiz-Fuertes, D. Martinez-Garcia, B. Garcia-Domene, A. L. J. Pereira, F. J. Manjón, P. Rodríguez-Hernández, A. Muñoz, F. Piccinelli, M. Bettinelli, and C. Popescu, Compressibility systematics of calcite-type borates: An experimental and theoretical structural study on ABO_3 (A = Al, Sc, Fe, and In), J. Phys. Chem. C **118**, 4354 (2014).

[101] S. Wang, N. Ye, and K. R. Poeppelmeier, Flux growth and crystal structure refinement of calcite type borate $GaBO_3$, Crystals **5**, 252 (2015). number: 2 Publisher: Multidisciplinary Digital Publishing Institute

[102] D. Kovacheva and K. Petrov, Preparation of crystalline $ZnSnO_3$ from Li_2SnO_3 by low-temperature ion exchange, Solid State Ionics **109**, 327 (1998).

[103] C. A. Niedermeier, K. Ide, T. Katase, H. Hosono, and T. Kamiya, Shallow valence band of rutile GeO_2 and P-type doping, J. Phys. Chem. C **124**, 25721 (2020). publisher: American Chemical Society

[104] L. Bohaty, S. Haussühl, J. Liebertz, and S. Stähr, Single crystal growth and physical properties of cubic

$Zn_4O(BO_2)_6$, Z. für Kristall. - Cryst. Mater. **161**, 157 (1982).

[105] P. Liang and S.-Y. Li, Synthesis, characterization and standard molar enthalpies of formation of two zinc borates: 2ZnO·2B2O3 · 3H2O and ZnB_4O_7, J. Chem. Thermodyn. **139**, 105868 (2019).

[106] Y. Liu, C. Li, M. A. Ud Din, L. Tang, Y. Lin, and N. Cheng, Optical properties of Eu^{3+}/Pr^{3+} doped $Zn_4O(BO_2)_6$ synthesized by solid-state reaction, Ceram. Int. **48**, 15737 (2022).

[107] P. Norton, T. Braggins, and H. Levinstein, Impurity and lattice scattering parameters as determined from Hall and mobility analysis in n-type silicon, Phys. Rev. B **8**, 5632 (1973).

[108] C. J. H. Wort and R. S. Balmer, Diamond as an electronic material, Mater. Today **11**, 22 (2008).

[109] W. J. Choyke and G. Pensl, Physical properties of SiC, MRS Bull. **22**, 25 (1997).

[110] R. Weingärtner, P. J. Wellmann, M. Bickermann, D. Hofmann, T. L. Straubinger, and A. Winnacker, Determination of charge carrier concentration in *n*- and *p*-doped SiC based on optical absorption measurements, Appl. Phys. Lett. **80**, 70 (2002).

[111] E. C. H. Kyle, S. W. Kaun, P. G. Burke, F. Wu, Y.-R. Wu, and J. S. Speck, High-electron-mobility GaN grown on free-standing GaN templates by ammonia-based molecular beam epitaxy, J. Appl. Phys. **115**, 193702 (2014).

[112] B. Gunning, J. Lowder, M. Moseley, and W. Alan Doolittle, Negligible carrier freeze-out facilitated by impurity band conduction in highly p-type GaN, Appl. Phys. Lett. **101**, 082106 (2012).

[113] J. Zhang, J. Shi, D.-C. Qi, L. Chen, and K. H. L. Zhang, Recent progress on the electronic structure, defect, and doping properties of Ga_2O_3, APL Mater. **8**, 020906 (2020).

[114] K. Hirama, Y. Taniyasu, H. Yamamoto, and K. Kumakura, Control of n-type electrical conductivity for cubic boron nitride (c-BN) epitaxial layers by Si doping, Appl. Phys. Lett. **116**, 162104 (2020).

[115] B. He, W. J. Zhang, Y. S. Zou, Y. M. Chong, Q. Ye, A. L. Ji, Y. Yang, I. Bello, S. T. Lee, and G. H. Chen, Electrical properties of Be-implanted polycrystalline cubic boron nitride films, Appl. Phys. Lett. **92**, 102108 (2008).

[116] R. J. Kaplar, A. A. Allerman, A. M. Armstrong, M. H. Crawford, J. R. Dickerson, A. J. Fischer, A. G. Baca, and E. A. Douglas, Review—Ultra-wide-bandgap AlGaN power electronic devices, ECS J. Solid State Sci. Technol. **6**, Q3061 (2016).

[117] M. L. Nakarmi, K. H. Kim, J. Li, J. Y. Lin, and H. X. Jiang, Enhanced *p*-type conduction in GaN and AlGaN by Mg-δ-doping, Appl. Phys. Lett. **82**, 3041 (2003).

[118] B. P. Gunning, C. A. M. Fabien, J. J. Merola, E. A. Clinton, W. A. Doolittle, S. Wang, A. M. Fischer, and F. A. Ponce, Comprehensive study of the electronic and optical behavior of highly degenerate p-type Mg-doped GaN and AlGaN, J. Appl. Phys. **117**, 045710 (2015).

[119] A. G. Baca, A. M. Armstrong, A. A. Allerman, E. A. Douglas, C. A. Sanchez, M. P. King, M. E. Coltrin, T. R. Fortune, and R. J. Kaplar, An $AlN/Al_{0.85}Ga_{0.15}N$ high electron mobility transistor, Appl. Phys. Lett. **109**, 033509 (2016).

[120] Y. Taniyasu, M. Kasu, and T. Makimoto, Increased electron mobility in n-type Si-doped AlN by reducing dislocation density, Appl. Phys. Lett. **89**, 182112 (2006).

[121] Y.-N. Xu and W. Y. Ching, Calculation of ground-state and optical properties of boron nitrides in the hexagonal, cubic, and wurtzite structures, Phys. Rev. B **44**, 7787 (1991).

[122] M.-Z. Huang and W. Y. Ching, A minimal basis semi-ab initio approach to the band structures of semiconductors, J. Phys. Chem. Solids **46**, 977 (1985).

[123] R. de Paiva and S. Azevedo, Cubic $(BN)_x$ $C_{2(1-x)}$ ordered alloys: A first-principles study of the structural, electronic, and effective mass properties, J. Phys.: Condens. Matter **18**, 3509 (2006).

[124] C.-X. Wang, G.-W. Yang, T.-C. Zhang, H.-W. Liu, Y.-H. Han, J.-F. Luo, C.-X. Gao, and G.-T. Zou, High-quality heterojunction between *p*-type diamond single-crystal film and *n*-type cubic boron nitride bulk single crystal, Appl. Phys. Lett. **83**, 4854 (2003).

[125] D. T. F. Marple, Effective electron mass in CdTe, Phys. Rev. **129**, 2466 (1963).

[126] R. Triboulet and Y. Marfaing, Growth of high purity CdTe single crystals by vertical zone melting, J. Electrochem. Soc. **120**, 1260 (1973).

[127] F. Nava, C. Canali, C. Jacoboni, L. Reggiani, and S. F. Kozlov, Electron effective masses and lattice scattering in natural diamond, Solid State Commun. **33**, 475 (1980).

[128] A. G. Redfield, Electronic Hall effect in diamond, Phys. Rev. **94**, 526 (1954).

[129] J. Isberg, J. Hammersberg, E. Johansson, T. Wikström, D. J. Twitchen, A. J. Whitehead, S. E. Coe, and G. A. Scarsbrook, High carrier mobility in single-crystal plasma-deposited diamond, Science **297**, 1670 (2002).

[130] M. Nesladek, A. Bogdan, W. Deferme, N. Tranchant, and P. Bergonzo, Charge transport in high mobility single crystal diamond, Diamond Relat. Mater. Proc. Diamond 2007, the 18th Eur. Conf. Diamond, Diamond-Like Mater., Carbon Nanotubes, Nitrides and Silicon Carbide **17**, 1235 (2008).

[131] L. S. Pan, D. R. Kania, P. Pianetta, J. W. Ager, M. I. Landstrass, and S. Han, Temperature dependent mobility in single-crystal and chemical vapor-deposited diamond, J. Appl. Phys. **73**, 2888 (1993).

[132] C. Janowitz, V. Scherer, M. Mohamed, A. Krapf, H. Dwelk, R. Manzke, Z. Galazka, R. Uecker, K. Irmscher, R. Fornari, M. Michling, D. Schmeißer, J. R. Weber, J. B. Varley, and C. G. V. de Walle, Experimental electronic structure of In_2O_3 and Ga_2O_3, New J. Phys. **13**, 085014 (2011).

[133] K. Irmscher, Z. Galazka, M. Pietsch, R. Uecker, and R. Fornari, Electrical properties of β-Ga_2O_3 single crystals grown by the Czochralski method, J. Appl. Phys. **110**, 063720 (2011).

[134] J. S. Blakemore, Semiconducting and other major properties of gallium arsenide, J. Appl. Phys. **53**, R123 (1982).

[135] M. Cardona, Electron effective masses of InAs and GaAs as a function of temperature and doping, Phys. Rev. **121**, 752 (1961).

[136] J.-M. Jancu, R. Scholz, E. A. de Andrada e Silva, and G. C. La Rocca, Atomistic spin-orbit coupling and k •

p parameters in III-V semiconductors, Phys. Rev. B **72**, 193201 (2005).
[137] P. Blood, Electrical properties of n-type epitaxial GaAs at high temperatures, Phys. Rev. B **6**, 2257 (1972).
[138] H. G. B. Hicks and D. F. Manley, High purity GaAs by liquid phase epitaxy, Solid State Commun. **7**, 1463 (1969).
[139] H. Miki and M. Otsubo, High purity GaAs crystals grown by liquid phase epitaxy, Jpn. J. Appl. Phys. **10**, 509 (1971).
[140] M. Asif Khan, Q. Chen, C. J. Sun, M. Shur, and B. Gelmont, Two-dimensional electron gas in GaN–AlGaN heterostructures deposited using trimethylamine-alane as the aluminum source in low pressure metalorganic chemical vapor deposition, Appl. Phys. Lett. **67**, 1429 (1995).
[141] V. W. L. Chin, T. L. Tansley, and T. Osotchan, Electron mobilities in gallium, indium, and aluminum nitrides, J. Appl. Phys. **75**, 7365 (1994).
[142] M. E. Levinshtein, S. L. Rumyantsev, and M. S. Shur, *Properties of Advanced Semiconductor Materials: GaN, AlN, InN, BN, SiC, SiGe* (John Wiley & Sons, New York, 2001).
[143] M. Feneberg, J. Nixdorf, C. Lidig, R. Goldhahn, Z. Galazka, O. Bierwagen, and J. S. Speck, Many-electron effects on the dielectric function of cubic In_2O_3: Effective electron mass, band nonparabolicity, band gap renormalization, and Burstein-Moss shift, Phys. Rev. B **93**, 045203 (2016).
[144] Y. Yoshida, D. M. Wood, T. A. Gessert, and T. J. Coutts, High-mobility, sputtered films of indium oxide doped with molybdenum, Appl. Phys. Lett. **84**, 2097 (2004).
[145] I. Hamberg and C. G. Granqvist, Evaporated Sn-doped In_2O_3 films: Basic optical properties and applications to energy-efficient windows, J. Appl. Phys. **60**, R123 (1986).
[146] R. L. Weiher, Electrical properties of single crystals of indium oxide, J. Appl. Phys. **33**, 2834 (1962).
[147] R. Clanget, Ionized impurity scattering in degenerate In_2O_3, Appl. Phys. **2**, 247 (1973).
[148] T. Koida and M. Kondo, High electron mobility of indium oxide grown on yttria-stabilized zirconia, J. Appl. Phys. **99**, 123703 (2006).
[149] T. Koida, Y. Ueno, and H. Shibata, In_2O_3-based transparent conducting oxide films with high electron mobility fabricated at low process temperatures, Phys. Status Solidi (a) **215**, 1700506 (2018).
[150] A. N. Chantis, M. van Schilfgaarde, and T. Kotani, *Ab Initio* Prediction of Conduction Band Spin Splitting in Zinc Blende Semiconductors, Phys. Rev. Lett. **96**, 086405 (2006).
[151] V. V. Galavanov and N. V. Siukaev, On mechanism of electron scattering in InP, Phys. Status Solidi (b) **38**, 523 (1970).
[152] L. D. Zhu, K. T. Chan, and J. M. Ballantyne, Very high mobility InP grown by low pressure metalorganic vapor phase epitaxy using solid trimethylindium source, Appl. Phys. Lett. **47**, 47 (1985).
[153] Y. Pei, Z. M. Gibbs, A. Gloskovskii, B. Balke, W. G. Zeier, and G. J. Snyder, Optimum carrier concentration in n-type PbTe thermoelectrics, Adv. Energy Mater. **4**, 1400486 (2014).
[154] R. S. Allgaier and W. W. Scanlon, Mobility of electrons and holes in PbS, PbSe, and PbTe between room temperature and 4.2°K, Phys. Rev. **111**, 1029 (1958).
[155] J. N. Zemel, J. D. Jensen, and R. B. Schoolar, Electrical and optical properties of epitaxial films of PbS, PbSe, PbTe, and SnTe, Phys. Rev. **140**, A330 (1965).
[156] A. D. LaLonde, Y. Pei, and G. Jeffrey Snyder, Reevaluation of $PbTe_{1-x}I_x$ as high performance n-type thermoelectric material, Energy Environ. Sci. **4**, 2090 (2011).
[157] Y. Pei, A. D. LaLonde, H. Wang, and G. Jeffrey Snyder, Low effective mass leading to high thermoelectric performance, Energy Environ. Sci. **5**, 7963 (2012).
[158] M. A. Green, Intrinsic concentration, effective densities of states, and effective mass in silicon, J. Appl. Phys. **67**, 2944 (1990).
[159] S. S. Li and W. R. Thurber, The dopant density and temperature dependence of electron mobility and resistivity in n-type silicon, Solid State Electron. **20**, 609 (1977).
[160] H. D. Barber, Effective mass and intrinsic concentration in silicon, Solid State Electron. **10**, 1039 (1967).
[161] R. A. Logan and A. J. Peters, Impurity effects upon mobility in silicon, J. Appl. Phys. **31**, 122 (1960).
[162] F. J. Morin and J. P. Maita, Electrical properties of silicon containing arsenic and boron, Phys. Rev. **96**, 28 (1954).
[163] R. Kaplan, R. J. Wagner, H. J. Kim, and R. F. Davis, Electron cyclotron resonance in cubic SiC, Solid State Commun. **55**, 67 (1985).
[164] J. Kono, S. Takeyama, H. Yokoi, N. Miura, M. Yamanaka, M. Shinohara, and K. Ikoma, High-field cyclotron resonance and impurity transition in *n*-type and *p*-type 3C-SiC at magnetic fields up to 175 T, Phys. Rev. B **48**, 10909 (1993).
[165] W. E. Nelson, F. A. Halden, and A. Rosengreen, Growth and properties of β-SiC single crystals, J. Appl. Phys. **37**, 333 (2004).
[166] M. Yamanaka, H. Daimon, E. Sakuma, S. Misawa, and S. Yoshida, Temperature dependence of electrical properties of *n*- and *p*-type 3C-SiC, J. Appl. Phys. **61**, 599 (1987).
[167] M. Shinohara, M. Yamanaka, H. Daimon, E. Sakuma, H. Okumura, S. Misawa, K. Endo, and S. Yoshida, Growth of high-mobility 3C-SiC epilayers by chemical vapor deposition, Jpn. J. Appl. Phys. **27**, L434 (1988).
[168] A. Suzuki, A. Uemoto, M. Shigeta, K. Furukawa, and S. Nakajima, Temperature dependence of electrical properties of non-doped and nitrogen-doped beta-SiC single crystals grown by chemical vapor deposition, Appl. Phys. Lett. **49**, 450 (1986).
[169] W. J. Schaffer, G. H. Negley, K. G. Irvine, and J. W. Palmour, Conductivity anisotropy in epitaxial 6H and 4H Sic, MRS Proc. **339**, 595 (1994).
[170] N. T. Son, O. Kordina, A. O. Konstantinov, W. M. Chen, E. Sörman, B. Monemar, and E. Janzén, Electron effective masses and mobilities in high-purity 6H–SiC chemical vapor deposition layers, Appl. Phys. Lett. **65**, 3209 (1994).
[171] R. Mickevičius and J. H. Zhao, Monte Carlo study of electron transport in SiC, J. Appl. Phys. **83**, 3161 (1998).
[172] B. Falabretti and J. Robertson, Electronic structures and doping of SnO_2, $CuAlO_2$, and $CuInO_2$, J. Appl. Phys. **102**, 123703 (2007).
[173] M. Dou and C. Persson, Comparative study of rutile and anatase SnO_2 and TiO_2: Band-edge structures, dielectric functions, and polaron effects, J. Appl. Phys. **113**, 083703 (2013).

[174] Z. Sroubek, Electron tunneling and band structure of $SrTiO_3$ and $KTaO_3$, Phys. Rev. B **2**, 3170 (1970).
[175] R. Moos, W. Menesklou, and K. H. Härdtl, Hall mobility of undoped n-type conducting strontium titanate single crystals between 19 K and 1373 K, Appl. Phys. A **61**, 389 (1995).
[176] O. N. Tufte and P. W. Chapman, Electron mobility in semiconducting strontium titanate, Phys. Rev. **155**, 796 (1967).
[177] M. Stamate, G. Lazar, and L. Iuliana, Anatase-rutile TiO_2 thin films deposited in a D.C. magnetron sputtering system, Rom. J. Phys. **53**, 217 (2008).
[178] Y. Yamada, H. Toyosaki, A. Tsukazaki, T. Fukumura, K. Tamura, Y. Segawa, K. Nakajima, T. Aoyama, T. Chikyow, T. Hasegawa, H. Koinuma, and M. Kawasaki, Epitaxial growth and physical properties of a room temperature ferromagnetic semiconductor: Anatase phase $Ti_{1-x}Co_xO_2$, J. Appl. Phys. **96**, 5097 (2004).
[179] L. Forro, O. Chauvet, D. Emin, L. Zuppiroli, H. Berger, and F. Lévy, High mobility *n*-type charge carriers in large single crystals of anatase (TiO_2), J. Appl. Phys. **75**, 633 (1994).
[180] K. J. Button, D. R. Cohn, M. von Ortenbert, B. Lax, E. Mollwo, and R. Helbig, Zeeman Splitting of Anomalous Shallow Bound States in ZnO, Phys. Rev. Lett. **28**, 1637 (1972).
[181] Y.-N. Xu and W. Y. Ching, Electronic, optical, and structural properties of some wurtzite crystals, Phys. Rev. B **48**, 4335 (1993).
[182] W. S. Baer, Faraday rotation in ZnO: Determination of the electron effective mass, Phys. Rev. **154**, 785 (1967).
[183] P. Wagner and R. Helbig, Halleffekt und anisotropie der beweglichkeit der elektronen in ZnO, J. Phys. Chem. Solids **35**, 327 (1974).
[184] D. C. Look, D. C. Reynolds, J. R. Sizelove, R. L. Jones, C. W. Litton, G. Cantwell, and W. C. Harsch, Electrical properties of bulk ZnO, Solid State Commun. **105**, 399 (1998).
[185] Y. Furubayashi, T. Hitosugi, Y. Yamamoto, K. Inaba, G. Kinoda, Y. Hirose, T. Shimada, and T. Hasegawa, A transparent metal: Nb-doped anatase TiO2, Appl. Phys. Lett. **86**, 252101 (2005).
[186] A. Bally, *Electronic Properties of Nano-Crystalline Titanium Dioxide Thin Films*, Ph.D. thesis, EPFL, Lausanne (1999).
[187] H. M. Manasevit, Single-crystal gallium arsenide on insulating substrates, Appl. Phys. Lett. **12**, 156 (1968).
[188] V. V. Afanas'ev, M. Houssa, A. Stesmans, and M. M. Heyns, Electron energy barriers between (100)Si and ultrathin stacks of SiO_2, Al_2O_3, and ZrO_2 insulators, Appl. Phys. Lett. **78**, 3073 (2001).
[189] C. Chen, M. Hong, J. Kwo, H. Cheng, Y. Huang, S. Lin, J. Chi, H. Lee, Y. Hsieh, and J. Mannaerts, Thin single-crystal Sc_2O_3 films epitaxially grown on Si (111)—structure and electrical properties, J. Cryst. Growth **278**, 638 (2005).